University of Arkansas, Fayetteville

ScholarWorks@UARK

5-2022

Photoassisted Nanoscale Memory Resistors

Amir Shariffar
University of Arkansas, Fayetteville

Follow this and additional works at: https://scholarworks.uark.edu/etd

Part of the Electrical and Electronics Commons, Nanoscience and Nanotechnology Commons, Nanotechnology Fabrication Commons, and the VLSI and Circuits, Embedded and Hardware Systems Commons

Photoassisted Nanoscale Memory Resistors

A dissertation submitted in partial fulfillment
of the requirements for the degree of
Doctor of Philosophy in Engineering

by

Amir Shariffar
University of Isfahan
Bachelor of Engineering in Electronics, 2013
Ruhr University of Bochum
Master of Science in Laser and Photonics, 2016

May 2022
University of Arkansas

This dissertation is approved for recommendation to the Graduate Council.

_____
Omar Manasreh, Ph.D.
Dissertation Director

_____   _____
Morgan E. Ware, Ph.D.   Jeff Dix, Ph.D.
Committee Member   Committee Member

_____
Bothina Manasreh, Ph.D.
Committee Member

Abstract

Memristors or memory resistors are promising two-terminal devices, which have the potential to revolutionize current electronic memory technologies. Memristors have been extensively investigated and reported to be practical devices, although they still suffer from poor stability, low retention time, and laborious fabrication processes.

The primary aim of this project was to achieve a device structure of quantum dots or thin films to address a fundamental challenge of unstable resistive switching behavior in memristors. Moreover, we aimed to investigate the effects of light illumination in terms of intensity and wavelength on the performance of the fabricated memristor. The parameters such as power consumption, retention time, endurance, and stability were investigated to determine the overall performance of the device. The experiment was designed and divided into three steps. First, a memristor was designed, fabricated, and characterized to explore the resistive switching mechanism in the device. Second, the same material used in the first step was incorporated into a photodetector, which was characterized to investigate the device photosensitivity, detectivity, responsivity, and photocurrent to dark current ratio. Finally, a new device was designed, fabricated, and characterized, which showed both memristivity and photodetectivity properties. The device is called a photomemristor since it has both functions of a memristor and a photodetector.

The "bottom-up" approach was used for fabricating the proposed memristor. In bottom-up methodology, nanostructures are synthesized and then assembled onto the substrate by stacking crystal planes onto each other. The fabricated memristors demonstrated bipolar resistive switching behavior with a low working voltage, efficient power consumption, and high endurance. We suggested the resistive switching mechanism of the device is related to the formation and rupture

of conducting filaments inside the switching layer of the memristor. Moreover, the conduction mechanism and electron transport in the switching layer of the device during the resistive switching process were analyzed. In addition, the effect of light illumination on the performance of the device was investigated and the SET voltage of the memristor was reduced as the light intensity increased. A gold-coated probe tip was used as the top electrode to confine the conductive filaments growth. The obtained results demonstrate significant improvement in the resistive switching behavior in terms of stability and uniformity compared to similar devices with larger electrode surface area.

This work provides new insights and suggests a measurement setup to further understand the resistive switching behavior in metal oxide and perovskite thin films for future applications of optoelectronic memristors in logic circuits, digital data storage, the internet of things, and neuromorphic computing.

Acknowledgements

Table of Contents

List of Figures

Abbreviations

HRS	High Resistance State
LRS	Low Resistance State
QDs	Quantum Dots
Si	Silicon
Au	Gold
Cr	Chromium
FTO	Fluorine-doped tin Oxide
DI	De-ionized
$CsPbBr_3$	Cesium Lead Bromide
ZnO	Zinc Oxide
NiO	Nickel Oxide
TiO_2	Titanium Oxide
Cu_2O	Cuprous Oxide
CuO	Cupric Oxide
O^{2-}	Oxygen ions
V_O^{++}	Oxygen Vacancy

Br^-	Bromide ions
V_{Br}^+	Bromide Vacancy
CF	Conductive Filament
e^-	Electrons
h^+	Holes
XRD	X-ray Diffraction
SEM	Scanning Electron Microscopy
I-V	Current-Voltage
UV-Vis	Ultraviolet-Visible
PL	Photoluminescence
Abs	Absorbance
E-beam	Electron Beam
FWHM	Full Width at Half Maximum

List of published papers

Chapter 2: A. Shariffar, H. Salman, T. A. Siddique, W. Gebril, and M. O. Manasreh, "Resistive switching in FTO/CuO–Cu$_2$O/Au memory devices," *Micro Nano Lett.*, vol. 15, no. 12, pp. 853–857, Oct. 2020, doi: 10.1049/mnl.2020.0300.

Chapter 3: A. Shariffar, H. Salman, T. A. Siddique, and M. O. Manasreh, "Effects of high-temperature annealing on the performance of copper oxide photodetectors," *Appl. Phys. A*, vol. 127, no. 10, p. 750, Oct. 2021, doi: 10.1007/s00339-021-04906-x.

Chapter 1: Introduction

Memristors (memory + resistor)

Memristor or memory resistor was first introduced by Leon Chua in 1971. He predicted the memristor as the fourth fundamental circuit element from the symmetry arguments. There are four fundamental circuit variables that are used to describe the relations between basic circuit elements, including resistor, capacitor, inductor, and memristor. These variables are electric voltage (v), current (i), charge (q), and magnetic flux (φ). A new parameter called Memristance (M) is defined to connect electric charge and magnetic flux in memristors, $d\varphi = M(q)dq$. If we substitute the equations on the boundaries shown in Figure 1.1, $d\varphi = vdt$ and $dq = idt$ into $d\varphi = M(q)dq$, we have $v = M(q)i$. If we assume a linear memristive system, memristance is a constant value that is identical to resistance. But, if memristance is a function of charge then we have a nonlinear dynamical system [1].
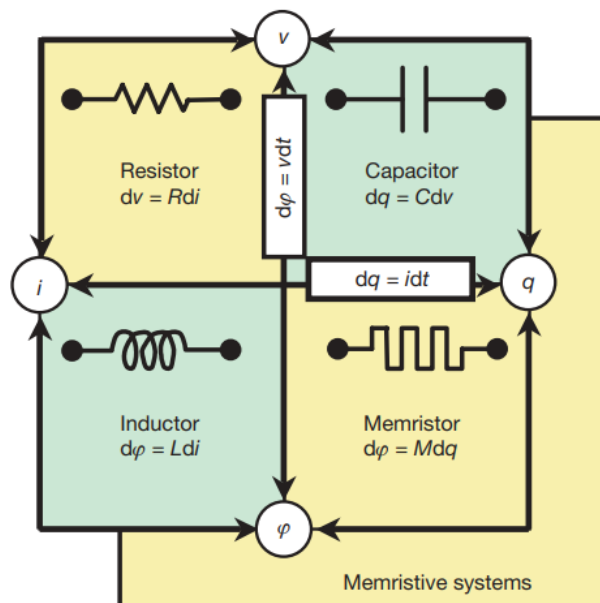
Figure 1.1. The basic circuit elements are described by relations between fundamental circuit variables.

There are two types of memristive systems, first, ionic thin film memristive systems that rely on the material properties and show pinched hysteresis by the application of electric fields. Second, magnetic memristive systems that rely on the electron spin and show pinched hysteresis by the application of magnetic fields. In this work, we focus on the ionic thin film memristive systems.

Memristors and human brain

The human brain can perform sophisticated computing tasks, like memorizing, learning, and recognition with extremely low energy consumption. Therefore, brain-inspired nanoscale devices can revolutionize information technology by mimicking the human brain. Achieving this goal requires introducing a scalable platform capable of reproducing the inherent functions of biological synapses in the human brain. To this aim, extensive efforts have been devoted to design and optimize a device able to emulate the "strength change" observed in human synapses [2]–[5]. The strength change refers to a process in which synapses are stimulated by neural spikes in such a way that the connection between two neurons is either facilitating or inhibiting through potentiation and depression mechanisms, respectively. This synapse's behavior is called "plasticity" and replication of synapses plasticity is the fundamental challenge to mimic the human brain. In a biological synapse, the ionic flow between two neurons can precisely adjust the synaptic strength, which enables the brain to learn and function [2], [4]. Therefore, the idea is to design and fabricate an optimal electronic device that can mimic the synaptic strength. Among electronic devices to emulate synapses, memristors have been investigated the most. A memristor (memory + resistor) is a two-terminal electronic device that features conductance change upon the application of electrical stimuli [6]. Memristors can perform as an artificial synapse by exploiting the same mechanisms to emulate the potentiation with increasing conductance and depression with

decreasing conductance. Similar to the synaptic strength, a memristor can modify its conductance from High Resistance State (HRS) to Low Resistance State (LRS) by controlling the charge flow through the device, this mechanism is called resistive switching (RS). The concept of using a memristor as an artificial synapse is shown in Figure 1.2(a). In short, neural spikes trigger vesicles holding chemical messengers called neurotransmitters, and vesicles move through the presynaptic neuron cell. Then, the vesicles merge with the neuron's membrane, spilling the neurotransmitters into the tiny space of 20-40 nm (synapse). Floating neurotransmitters move through the synapse and finally dock into the receptors to carry the message signal across the neurons [7]. Figure 1.2(b) demonstrates the magnified synaptic junction and the proposed memristor's general structure as an artificial synapse. The top and bottom electrodes resemble pre-and postsynaptic neurons, and the metal oxide layers resemble the gap or biological synapse. We can model neurotransmitters as oxygen vacancies or traps in the metal oxide layer. As we apply the bias voltage to the memristor, the oxygen vacancies form a conductive filament, and the device goes to the LRS state. On the other hand, as the bias polarity changes, oxygen vacancies move and break the filament, therefore the device switches back to the HRS state [8]. The resistive switching mechanism in different materials is still under debate and further investigations are required to improve the RS behavior in memristor-based artificial synapses [9]. Supported by recent studies on artificial synapses, researchers tend to improve the stability, endurance, and uniformity of the RS behavior in synaptic memristors. Specifically, the main challenge is to prevent sudden ruptures in the memristor's conductive filament (CFs) during the RS process [10]. To address these problems, different structures of metal oxide quantum dots (QDs) and thin films are investigated to control the formation of conductive filaments in memristors.

(a)

Presynaptic Neuron

Postsynaptic Neuron

Neural Spike

(b)

V

A

Electrode

Metal Oxide

Electrode

Presynaptic Neuron

Neurotransmitters

Synapse

Receptors

Postsynaptic Neuron

(c)

A

Memristor

V

(d)

LRS

HRS

SET

RESET
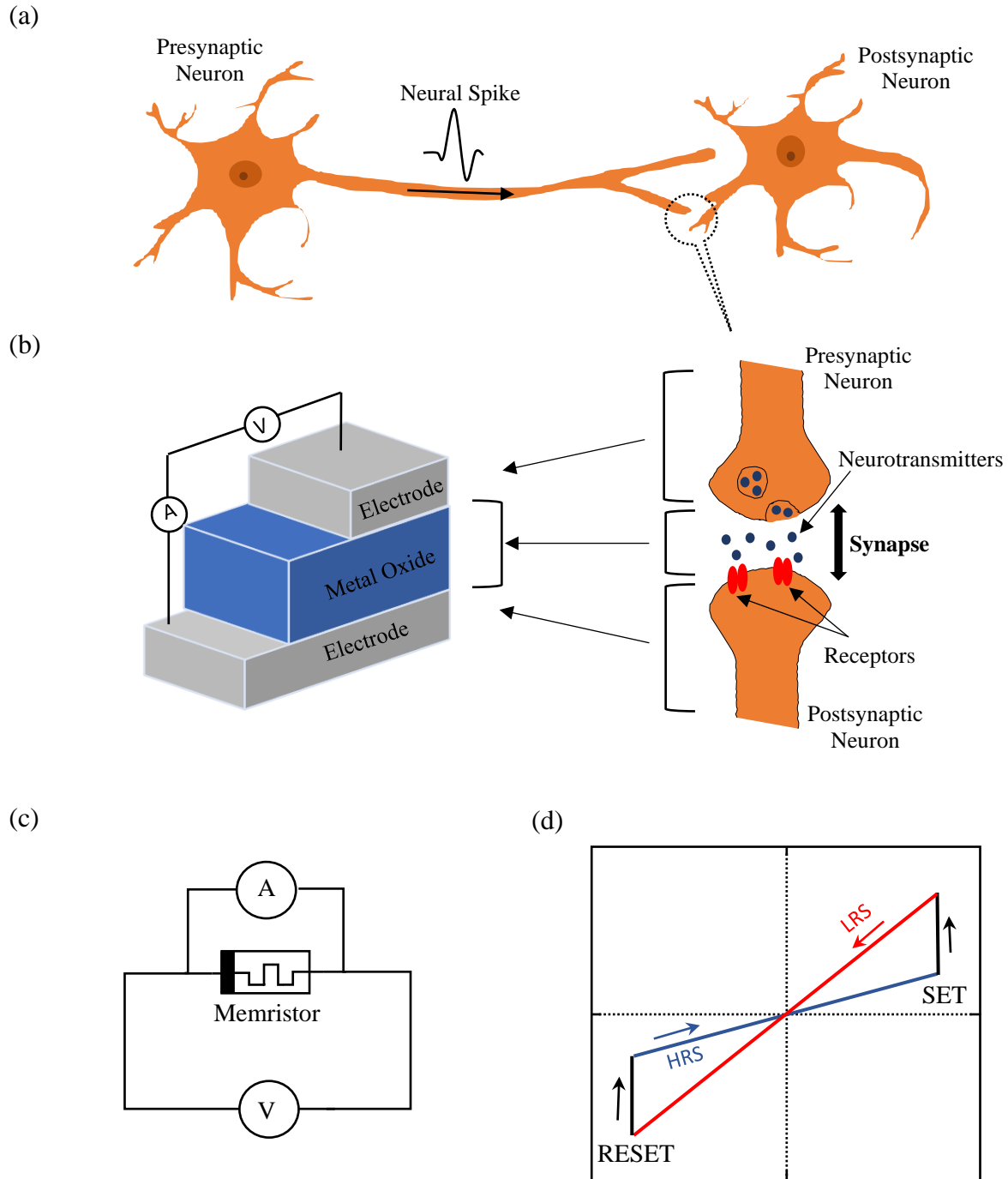
Figure 1.2. General schematics of a biological and artificial synapse. (a) Schematic diagram of presynaptic and postsynaptic neurons connected through a synapse. (b) A general structure of the memristor-based artificial synapse, inspired by a biological synapse. (c) The circuit model of the memristor and the measurement setup. (d) The resistive switching phenomena in theory.

Figure 1.2(c) illustrates the circuit model of a memristor and the measurement setup for I-

V characterization, which is expected to show the resistive switching phenomena shown in Figure

1.2(d). As the blue arrow indicates, in a positive voltage sweep, the device stays in the high resistance state (HRS) until an abrupt change occurs, and the device changes its state to the low resistance state (LRS). As the bias voltage sweeps back from positive to negative, the device maintains its state until another sudden current drop occurs at a negative voltage value, and the device resets back to HRS again. This cyclic mechanism is called memristive behavior because the device can memorize its resistance state. To analyze the performance of the fabricated memristor, the power consumption and following properties must be measured:

1- <u>Retention time</u>: the maximum time that the memristor can maintain its resistance state

2- <u>Endurance</u>: the maximum number of switching cycles in which the memristor shows consistent resistive switching behavior

3- <u>Stability</u>: the uniform transition between resistance states

Another important factor that determines the overall performance of a memristor is power consumption. The power consumption depends on the output current, set, and reset voltages. It can be challenging to reduce the set and reset voltages in memristors. For example, Figure 1.3(a) demonstrates a device made of titanium oxide (TiO_2) thin films sandwiched between gold (Au) and (Ti) electrodes. The device sets to LRS at -3.1 V in the negative voltage sweep, and in the positive voltage sweep, the device resets to HRS at +4 V. Thus, the set and reset voltages are high in this device which may not be useful in practical applications. Another example is shown in Figure 1.3(b), a device made of zinc oxide (ZnO) quantum dots sandwiched between Au and fluorine-doped tin oxide (FTO) electrodes. Regardless of high set and reset voltages, the current transitions between LRS and HRS are not uniform. Therefore, this device may not be applicable in practical memristive applications.

(a)
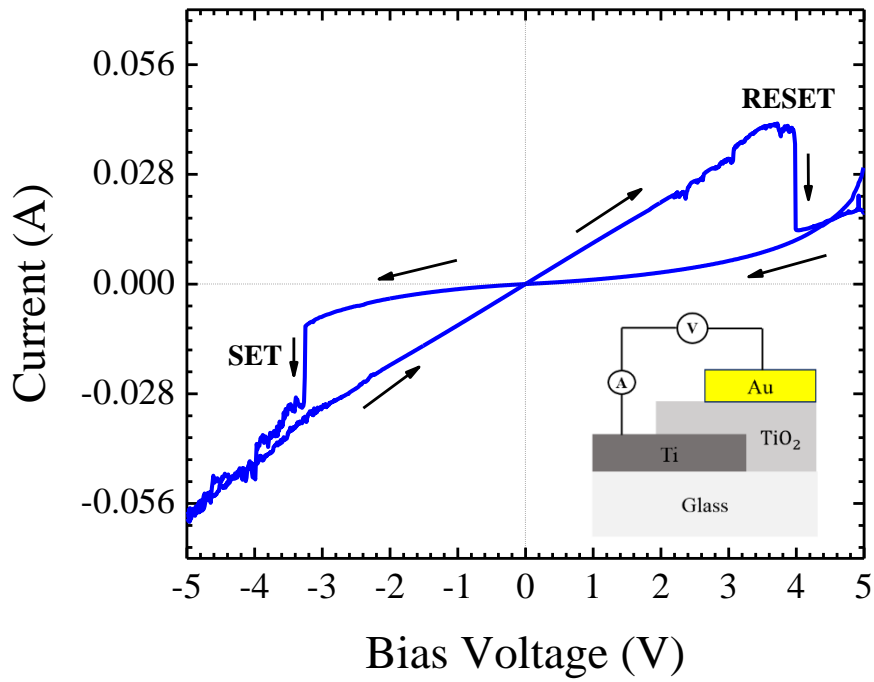
(b)
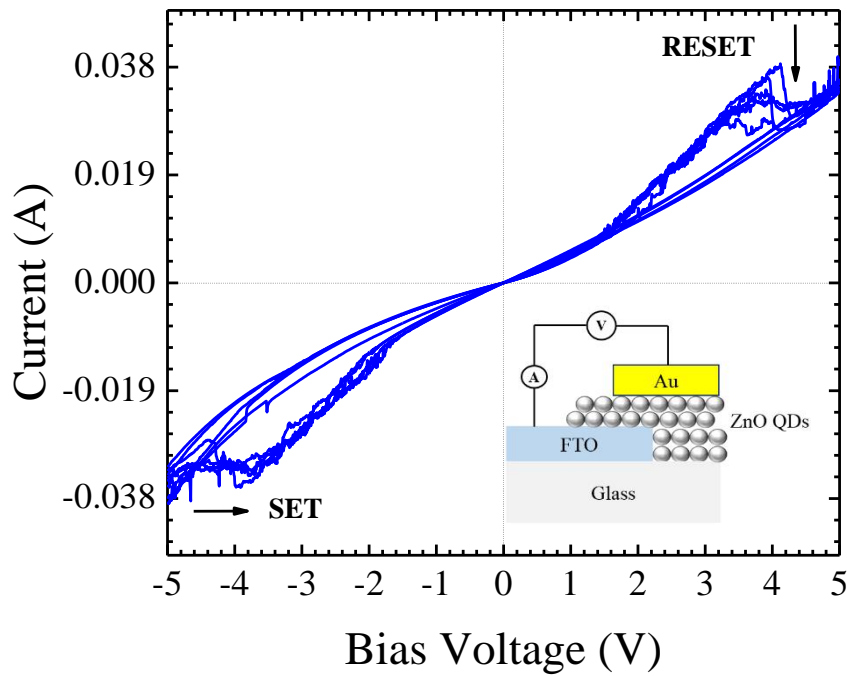
Figure 1.3. (a) Resistive switching behavior of a device made of titanium oxide (TiO$_2$) thin films sandwiched between gold (Au) and (Ti) electrodes. (b) Resistive switching behavior of a device made of zinc oxide (ZnO) quantum dots sandwiched between gold (Au) and (FTO) electrodes.

Applications

Memristors are widely used in non-volatile memory applications as they can retain data with low power consumptions [11]. Memristors can be used to mimic biological and neuromorphic systems. Memristor-based artificial synapses can highly contribute to the larger fields as they promise a significant impact on the electronics industry [12]. Specifically, memristors provide additional advantages over conventional memories such as low power consumption and higher storage density. Recently developed crossbar memristors are capable of power-efficient storage in a very small space, where they can address 128 TB of memory in one square centimeter [13]. Therefore, the proposed project contributes to performance enhancement in electronic circuits from low power to remote sensing applications.

Specific aims

At the completion of this project, we aim to successfully achieve a device structure of quantum dots or metal oxide thin films to address a fundamental challenge of unstable resistive switching behavior in memristors. Moreover, we aim to investigate the effects of light illumination in terms of intensity and wavelength on the performance of the fabricated memristor. The parameters such as power consumption, retention time, endurance, and stability determine the overall performance of the device. In the following, we introduce research objectives that facilitate the achievement of our aims.

1. To investigate the underlying factors that cause unstable resistive switching in memristors

2. To assess current strategies to stabilize resistive switching behavior in memristors

3. To explore the effect of various thin films or quantum dots on the memristor's performance

4. To investigate a method in which a gold-coated probe tip used as a top electrode

5. To investigate the effects of light illumination on the performance of a memristor

6. To evaluate and compare the performance of the fabricated memristors

7. To identify the optimal memristor's structure and proceed to the optimization process

Therefore, we can design and analyze our experiments in the following steps shown in Figure 1.4. The synthesized materials shown in Table 1 are used to fabricate multiple devices with different structures, dimensions, and applications. In the first step, a memristor is designed, fabricated and characterized to explore the resistive switching behavior of the device. The same material is used in the second step to fabricate a photodetector which is characterized to investigate the device photosensitivity, detectivity, responsivity, and photocurrent to dark current ratio. In the third step, a new device is designed, fabricated, and characterized which shows both memristivity and photodetectivity properties. The device is called a photomemristor since it has both functions of a memristor and a photodetector.

Step 1: Memristor

Step 2: Photodetector

Step 3: Photomemristor
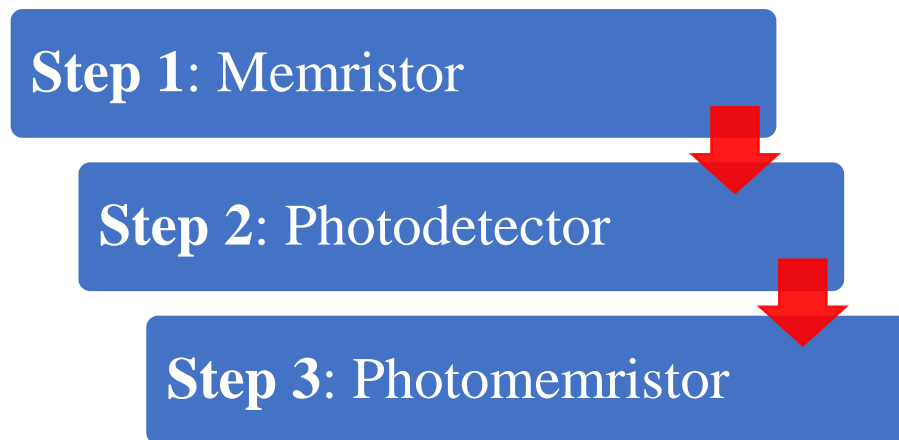
Figure 1.4. The experimental design is divided into three steps of design and fabrication of memristors, photodetectors, and photomemristors.

Research strategy

In this work, we use a "bottom-up" approach for fabricating the proposed memristor. In the bottom-up methodology, nanostructures such as quantum dots or thin films are synthesized

and then assembled onto the substrate by stacking crystal planes onto each other. A bottom-up approach can promise nanostructures with uniform and homogenous chemical compositions [14]. We divide the experiment into four steps to explore the effect of individual variables. In the first step of this experiment, we synthesize different types of quantum dots and thin films listed in Table 1. The listed materials have been separately used for memristive applications [15], [16].

Table 1. Types and properties of required QDs and thin films for the experiment.

Material	Synthesis	Intrinsic Type	Size or Thickness
Zinc Oxide (ZnO)	QDs	n-type	10 nm in diameter
Molybdenum trioxide (MoO_3)	QDs	p-type	5 nm in diameter
Titanium dioxide (TiO_2)	thin films	n-type	60 nm in thickness
Copper Oxide (CuO)	thin films	p-type	100 nm in thickness
Nickel Oxide (NiO)	QDs	p-type	5 nm in diameter
Hafnium dioxide (HfO_2)	QDs, thin films	n-type	50 nm in thickness
Cesium lead bromide (CsPbBr3)	QDs, thin films	p-type	60 nm in thickness

In the second step, we evaluate the quality, size, and thickness of synthesized QDs and thin films. To this aim, we use scanning electron microscopy (SEM) to explore the size and thickness of synthesized materials. Besides, X-ray diffraction (XRD) is used to characterize elements constituting the material and crystal structure. The third step is to fabricate the proposed devices, in which the active layer is either a single layer or composed of one type of quantum dots and the opposite type of thin films for each device. We employ a fluorine-doped tin oxide (FTO) glass substrate as the bottom electrode. Then, we use the spin-coating deposition technique to grow the active layers of QDs or thin films for each device, followed by the top electrode metallization using the electron beam deposition system at room temperature and the pressure of 5×10^{-6} Torr. In the last step, we test and analyze the performance of the fabricated device using the Keithley 4200 SCS parameter analyzer and the solar simulator. The current-voltage (I-V) characterization shows the resistive switching behavior including, endurance, uniformity, retention time, and on/off ratio. After collecting data from all devices with different structures, we analyze the memristor's

performance and identify the optimal memristor's structure. At the end of this experiment, we evaluate the proposed hypothesis, and then we proceed to the optimization process.

In the chapter 1, we report a stable and power-efficient memristor with a novel structure and facile fabrication based on CuO-Cu$_2$O complex thin films. The fabricated memristor consists of CuO-Cu$_2$O complex thin films as a switching layer, which is sandwiched between FTO and deposited gold (Au) electrodes. The FTO as the bottom electrode acts as an oxygen vacancy reservoir where oxygen vacancies can be stored or supplied during the resistive switching [17]. Moreover, FTO can tolerate high annealing temperatures without increasing the sheet resistance during copper oxidization [17]. Au electrodes are deposited on top of the device because compared to platinum (Pt) the Au contact is less expensive and demonstrates higher endurance [18]. Structural and memristive properties are characterized using Raman spectroscopy, UV-Vis absorbance, and current-voltage (I-V) measurements. The memristivity is identified by the pinch hysteresis loop and switching cycles from the high resistance state (HRS) to the low resistance state (LRS). The memristor possesses a low operation voltage, high endurance, and uniformity. Moreover, the carrier transport mechanisms have been investigated, suggesting the space charge limited conduction (SCLC) to be the main conduction mechanism. In the chapter 2, we deploy copper oxide thin films to develop UV-Visible photodetectors. The fabricated devices are characterized in terms of photosensitivity, detectivity, and responsivity.

In the chapter 4, we design an optoelectronic memory device that functions as a memristor and photodetector simultaneously. The proposed device has two inputs (light, voltage) and one output (current). The resistive switching behavior of the memristor can be adjusted using light illumination and voltage polarity. Figure 1.5(a) demonstrates a block diagram of the proposed device, and a schematic picture of the fabricated device is shown in Figure 1.5(b). We aim to

confine conductive filaments growth, which is highly localized, depending on the contact size between the switching layer and top electrode. Therefore, the idea is to minimize the contact area by applying a gold-coated probe tip onto the surface of the switching layer instead of depositing top electrodes. The proposed device must be cost-effective with a simple structure and a facile fabrication method. To this aim, we synthesized and characterized various types of perovskite thin films and quantum dots incorporated into the device. For example, perovskite materials are widely used for nonvolatile memristors [19]. Cesium lead bromide ($CsPbBr_3$) thin films and quantum dots show promising characterization results in terms of photosensitivity, detectivity, and responsivity as they are investigated in our previous work [20]. Therefore, we focus on $CsPbBr_3$ as a building material in the device that we proposed.

(a)
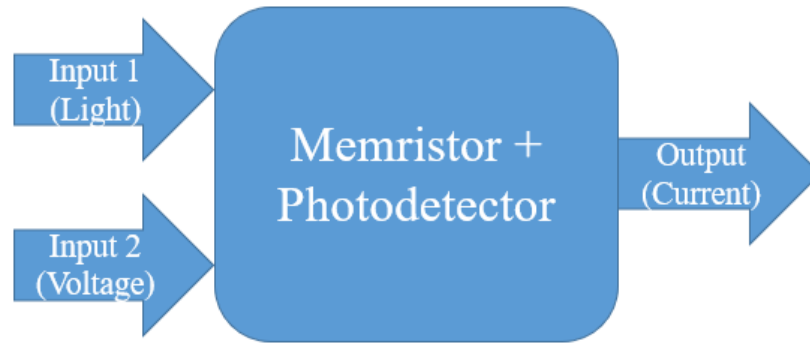
(b)
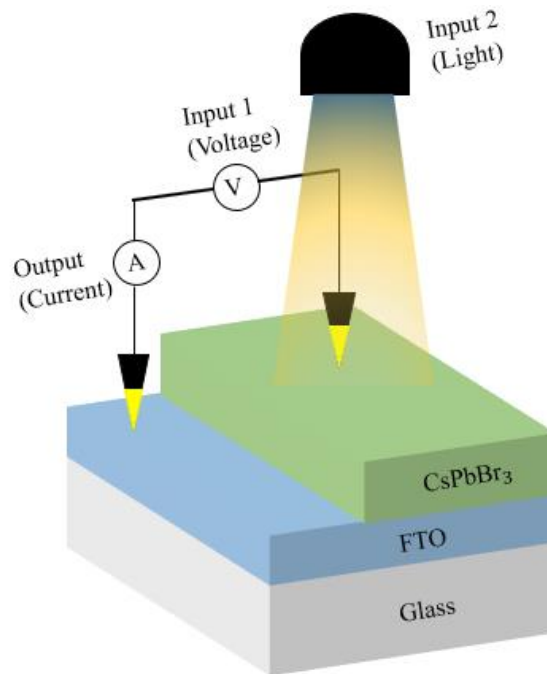
Figure 1.5. (a) A block diagram of the proposed device. (b) A schematic picture of the fabricated device under light illumination with the adjustable intensity.

References

[1] L. Chua, "Memristor-The missing circuit element," *IEEE Trans. Circuit Theory*, vol. 18, no. 5, pp. 507–519, 1971, doi: 10.1109/TCT.1971.1083337.

[2] S. H. Jo, T. Chang, I. Ebong, B. B. Bhadviya, P. Mazumder, and W. Lu, "Nanoscale Memristor Device as Synapse in Neuromorphic Systems," *Nano Lett.*, vol. 10, no. 4, pp. 1297–1301, Apr. 2010, doi: 10.1021/nl904092h.

[3] C. Sung, H. Hwang, and I. K. Yoo, "Perspective: A review on memristive hardware for neuromorphic computation," *J. Appl. Phys.*, vol. 124, no. 15, p. 151903, Oct. 2018, doi: 10.1063/1.5037835.

[4] S. G. Kim, J. S. Han, H. Kim, S. Y. Kim, and H. W. Jang, "Recent Advances in Memristive Materials for Artificial Synapses," *Adv. Mater. Technol.*, vol. 3, no. 12, p. 1800457, Dec. 2018, doi: 10.1002/admt.201800457.

[5] Y. Li *et al.*, "Ultrafast Synaptic Events in a Chalcogenide Memristor," *Sci. Rep.*, vol. 3, no. 1, p. 1619, Dec. 2013, doi: 10.1038/srep01619.

[6] D. B. Strukov, G. S. Snider, D. R. Stewart, and R. S. Williams, "The missing memristor found," *Nature*, vol. 453, no. 7191, pp. 80–83, May 2008, doi: 10.1038/nature06932.

[7] Z. Wang *et al.*, "Memristors with diffusive dynamics as synaptic emulators for neuromorphic computing," *Nat. Mater.*, vol. 16, no. 1, pp. 101–108, Jan. 2017, doi: 10.1038/nmat4756.

[8] Y. Li, S. Long, Q. Liu, H. Lv, and M. Liu, "Resistive Switching Performance Improvement via Modulating Nanoscale Conductive Filament, Involving the Application of Two-Dimensional Layered Materials," *Small*, vol. 13, no. 35, p. 1604306, Sep. 2017, doi: 10.1002/smll.201604306.

[9] S. H. Tan, P. Lin, H. Yeon, S. Choi, Y. Park, and J. Kim, "Perspective: Uniform switching of artificial synapses for large-scale neuromorphic arrays," *APL Mater.*, vol. 6, no. 12, p. 120901, Dec. 2018, doi: 10.1063/1.5049137.

[10] W. Sun *et al.*, "Understanding memristive switching via in situ characterization and device modeling," *Nat. Commun.*, vol. 10, no. 1, p. 3453, Dec. 2019, doi: 10.1038/s41467-019-11411-6.

[11] A. Shariffar, H. Salman, T. A. Siddique, W. Gebril, and M. O. Manasreh, "Resistive switching in FTO/CuO–Cu$_2$O/Au memory devices," *Micro Nano Lett.*, vol. 15, no. 12, pp. 853–857, Oct. 2020, doi: 10.1049/mnl.2020.0300.

[12] M. A. Zidan, J. P. Strachan, and W. D. Lu, "The future of electronics based on memristive systems," *Nat. Electron.*, vol. 1, no. 1, pp. 22–29, Jan. 2018, doi: 10.1038/s41928-017-0006-8.

[13] P. O. Vontobel, W. Robinett, P. J. Kuekes, D. R. Stewart, J. Straznicky, and R. Stanley Williams, "Writing to and reading from a nano-scale crossbar memory based on memristors," *Nanotechnology*, vol. 20, no. 42, p. 425204, Oct. 2009, doi: 10.1088/0957-4484/20/42/425204.

[14] *Fundamentals of Nanoparticles*. Elsevier, 2018. doi: 10.1016/C2016-0-01899-5.

[15] S. Stathopoulos *et al.*, "Multibit memory operation of metal-oxide bi-layer memristors," *Sci. Rep.*, vol. 7, no. 1, p. 17532, Dec. 2017, doi: 10.1038/s41598-017-17785-1.

[16] B. Mohammad *et al.*, "State of the art of metal oxide memristor devices," *Nanotechnol. Rev.*, vol. 5, no. 3, Jan. 2016, doi: 10.1515/ntrev-2015-0029.

[17] J. K. Yang, B. Liang, M. J. Zhao, Y. Gao, F. C. Zhang, and H. L. Zhao, "Reference of Temperature and Time during tempering process for non-stoichiometric FTO films," *Sci. Rep.*, vol. 5, no. 1, p. 15001, Dec. 2015, doi: 10.1038/srep15001.

[18] Y. Khrapovitskaya, N. Maslova, I. Sokolov, Y. Grishchenko, D. Mamichev, and M. Zanaveskin, "The titanium oxide memristor contact material's influence on element's cyclic stability to degradation: The titanium oxide memristor contact material's influence on element's cyclic stability to degradation," *Phys. Status Solidi C*, vol. 12, no. 1–2, pp. 202–205, Jan. 2015, doi: 10.1002/pssc.201400109.

[19] X. Xiao *et al.*, "Recent Advances in Halide Perovskite Memristors: Materials, Structures, Mechanisms, and Applications," *Adv. Mater. Technol.*, vol. 5, no. 6, p. 1900914, Jun. 2020, doi: 10.1002/admt.201900914.

[20] H. Salman, A. Shariffar, T. A. Siddique, W. Jibreel, A. Kuchuk, and M. O. Manasreh, "CsPbBr $_3$ perovskite photodetector with interdigital chromium electrodes," *Eng. Res. Express*, vol. 2, no. 4, p. 045011, Dec. 2020, doi: 10.1088/2631-8695/abbf90.

Chapter 2: Resistive switching in FTO/CuO–Cu₂O/Au memory devices

Abstract

Memristors are considered to be next-generation non-volatile memory devices owing to their fast switching and low power consumption. Metal oxide memristors have been extensively investigated and reported to be promising devices, although they still suffer from poor stability and laborious fabrication process. Herein, we report a stable and power-efficient memristor with novel heterogeneous electrode's structure and facile fabrication based on CuO-Cu₂O complex thin films. The proposed structure of the memristor contains an active complex layer of cupric oxide (CuO) and cuprous oxide (Cu₂O) sandwiched between fluorine-doped tin oxide (FTO) and gold (Au) electrodes. The fabricated memristors demonstrate bipolar resistive switching (RS) behavior with a low working voltage (~1 V), efficient power consumption, and high endurance over 100 switching cycles. We suggest the RS mechanism of the proposed device is related to the formation and rupture of conducting filaments inside the memristor. Moreover, we analyze the conduction mechanism and electron transport in the active layer of the device during the RS process. Such a facile fabricated device has a promising potential for future memristive applications.

Introduction

The memristor (memory + resistor) was first proposed by Leon Chua in 1971 as the fourth fundamental circuit element [1]. A typical structure of two-terminal memristors consists of a switching layer sandwiched between two metallic electrodes. Depending on the switching layer properties, memristors are classified as bulk, interface, and filament types. The filament-type

memristors continue to attract more research attention due to their superior performance. Among filament types memristors, metal oxides are the most commonly used materials in which oxygen vacancies form conductive filaments that are responsible for resistive switching behavior [2]. There have been several studies on metal-oxide memristors such as TiO_2 [3], HfO_2 [4], ZnO [5], AlO_x [6], WO_x [7], TaO_x [8], etc. Moreover, cupric oxide (CuO) has been also reported to show bipolar memristive behavior [9]–[11]. In copper oxide memristors, the active layer is often made by thermal annealing [12], or solution processing [13], which features inexpensive and low-power operation [14]. The facile fabrication of copper oxide memristors is an advantage over other types of metal oxide memristors however, further efforts are required to improve the stability, endurance, and retention time during the RS mechanism [15], [16].

In this work, we report a stable and power-efficient memristor with a novel structure and facile fabrication based on CuO-Cu_2O complex thin films. The fabricated memristor consists of CuO-Cu_2O complex thin films as a switching layer, which is sandwiched between FTO and deposited gold (Au) electrodes. The FTO as the bottom electrode acts as an oxygen vacancy reservoir where oxygen vacancies can be stored or supplied during the resistive switching [17]. Moreover, FTO can tolerate high annealing temperatures without increasing the sheet resistance during copper oxidization [18]. Au electrodes are deposited on top of the device because compared to platinum (Pt) the Au contact is less expensive and demonstrates higher endurance [19]. Structural and memristive properties are characterized using Raman spectroscopy, UV-Vis absorbance, and current-voltage (I-V) measurements. The memristivity is identified by the pinch hysteresis loop and switching cycles from the high resistance state (HRS) to the low resistance state (LRS). The memristor possesses a low operation voltage, high endurance, and uniformity.

Moreover, the carrier transport mechanisms have been investigated, suggesting the space charge limited conduction (SCLC) to be the main conduction mechanism.

Fabrication and experimental methods

A 100 nm-thick copper (Cu) thin film was deposited on the FTO substrate using electron beam evaporation at room temperature. The vacuum pressure was kept at 6×10^{-6} Torr during the deposition process. The as-deposited Cu metal film was annealed at 400 °C for 45 minutes in an oxygen ambient environment to form the copper oxide thin film. The fabrication process of the device is shown in Figure 2.1. We used Horiba LabRam micro-Raman spectrometer and Cary 500 UV-Vis-NIR Spectrophotometer to characterize the Raman and absorbance properties of the thin film, respectively. The Raman measurements are performed using a continuous red (632 nm) laser as the excitation source. The elastically scattered light is filtered out to detect the weaker inelastically scattered light from optical phonons. The Raman spectrum is recorded in the range of 200 - 700 cm^{-1} to confirm the presence of copper oxide elements by comparing the position of phonon modes with existing literature. We also measured the absorbance of the grown thin films in the wavelength range of 300 – 800 nm, where the excitonic peak and bandgap of the copper oxide can be observed. To achieve FTO/CuO-Cu_2O/Au devices, the 50 nm-thick circle gold (Au) electrodes with different areas were deposited using a shadow mask and electron beam evaporation. We used the Keithley 4200 SCS parameter analyzer and a probe station for the current-voltage I-V characterization of fabricated devices. For each device on the sample, we applied the consecutive external DC voltages with different polarities between the Au and FTO as top and bottom electrodes. The bias voltage is sweeping between +5 V and -5 V while the output current is measured. All the measurements were performed at room temperature.
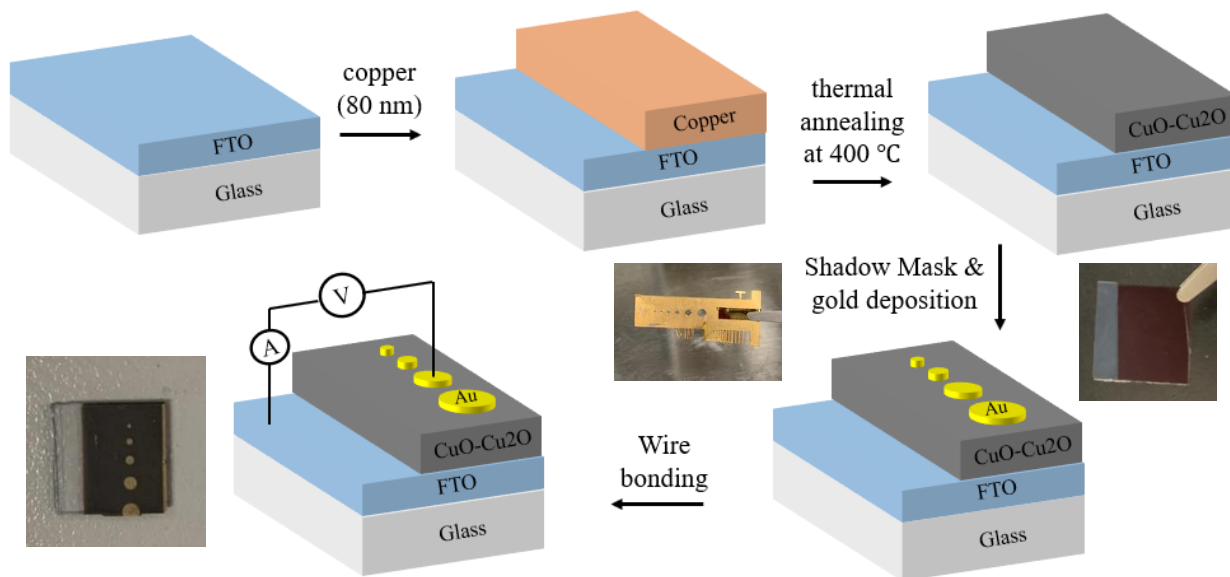
Figure 2.1. The fabrication process of FTO/CuO-Cu$_2$O/Au devices.

Results and discussions

Figure 2.2 plots the Raman scattering spectra of the grown copper oxide thin film. The three peaks at 307 cm^{-1}, 355 cm^{-1}, and 640 cm^{-1} are the Raman fingerprints of CuO, which is consistent with relevant studies [20], [21]. These strong peaks are assigned to A$_g$, B$_g$, and 2B$_g$ phonon modes, which can shift slightly depending on the annealing temperature of CuO [22]. There are also broad humps between 390 cm^{-1} and 640 cm^{-1}, which indicate the presence of cuprous oxide (Cu$_2$O) phase [23]. Therefore, the prepared copper oxide thin film contains both CuO and Cu$_2$O phases. Figure 2.3 shows the optical absorption of CuO-Cu$_2$O complex thin films annealed at 400C$^{\circ}$. The thin films exhibit high absorbance in the UV region centered around 350 nm. The obtained indirect bandgap using the Tauc plot is 1.45 eV that is within the range reported by [24], [25].
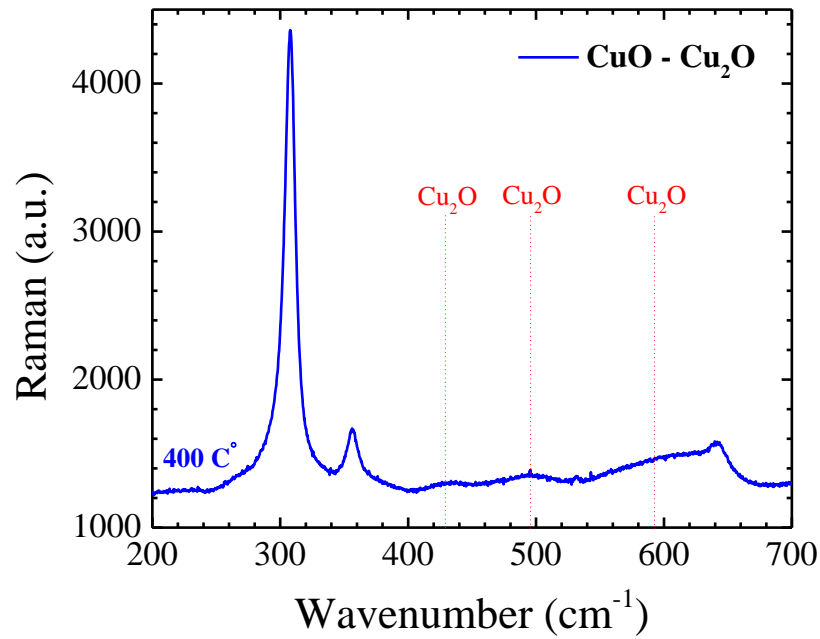
Figure 2.2. The Raman scattering spectra of CuO-Cu$_2$O thin films excited by the red laser.
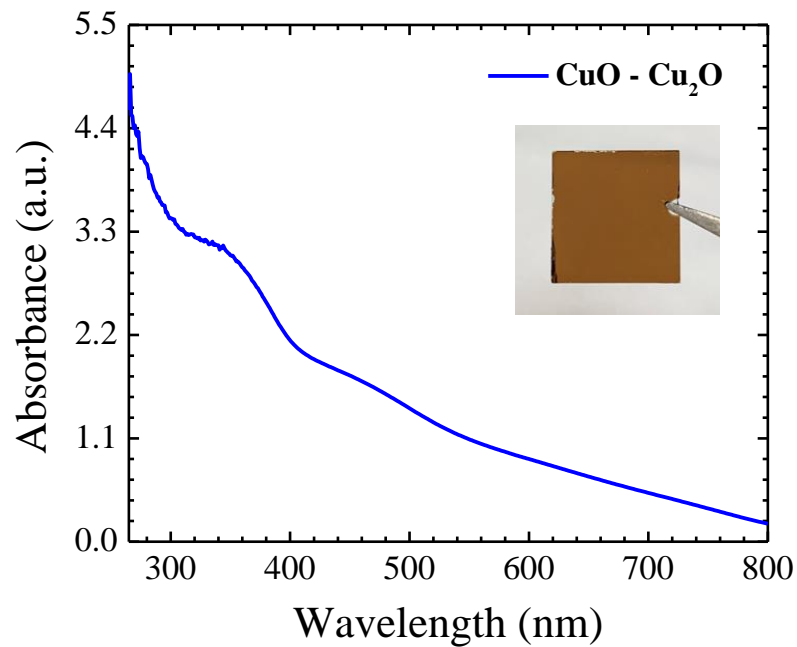
Figure 2.3. The absorbance spectra of CuO-Cu$_2$O thin films. The inset demonstrates the Tauc plot representing the extrapolation of the linear part of the curve to achieve the indirect bandgap of CuO-Cu$_2$O thin films.

A schematic picture and the structure of two-terminal memory devices studied in this work are shown in Figure 2.4(a). Before performing I-V measurements, the electroforming process is required to create a sufficiently strong electric field and initiate a soft breakdown of the switching layer in the device. As a result, massive oxygen vacancies are introduced into the copper oxide layer, which can form nanoscale conductive filaments [26]. To this aim, the applied voltage is slowly increased with a current compliance of 1 mA to protect the device from a permanent breakdown (not shown here). The electroforming process is observed at around -6 V, where the current suddenly increases and stabilizes afterward. Then, when we sweep back the voltage from negative to a positive value with a sweep rate of 10 mV/s, an abrupt current change occurs at approximately 3.2 V, indicating resistive switching (RS) from an initial low resistance state (LRS) to a high resistance state (HRS), which is called the "RESET" process. Subsequently, we sweep the voltage from positive to a negative value, and the device remains at HRS until another RS occurs around -1 V, and the device switches back from HRS to LRS, which is called the "SET" process. The memristive behavior of the device with the smallest electrode's diameter of 0.2 mm can be observed from the measured current-voltage (I-V) characteristics shown in Figure 2.4(b). We prepared multiple devices with different Au electrode areas, and the device with the smallest diameter of 0.2 mm exhibits the best performance. Devices with the larger Au electrode areas demonstrate poor performance in terms of endurance, retention time, and on/off ratio. A possible reason can be related to the local resistive switching in the device due to the formation of highly localized filaments [27]. As we expected, the I-V characteristics are asymmetric, which can be used to differentiate similar conduction mechanisms from each other [28]. By sweeping voltage repeatedly between positive and negative values, the I-V curves show little difference between first and last sweeping cycles, indicating high endurance and reproducibility up to 100 cycling

times (Figure 2.4(c)). Thus, the RS behavior is reversible and instantaneous, which is important for a reliable nonvolatile memory mechanism. However, the origin of RS mechanism is still in debate, relevant studies on copper-oxide based devices agree on the formation and rupture of conducting filaments with oxygen vacancies accumulation and depletion induced by applying the external voltage [29]. The scattered switching voltage distribution observed at OFF states in Fig. 3c is due to the rupture of filaments, either by ion migration or Joule heating [30]. Moreover, symmetric multilevel transitions occur at both HRS and LRS states around ± 1 V where the possible reason might be the hopping conduction in which the shallow trapped electrons can surpass the energy barrier and form the leakage current in discontinuous residual metallic filament [31]. This phenomenon can also suggest a multilevel data storage capability of the device [32]. Another advantage of this device is low power consumption (<4 µW), which is calculated by multiplying the reading voltage (0.2 V) and LRS current values (<20 µA) [33].

(a)
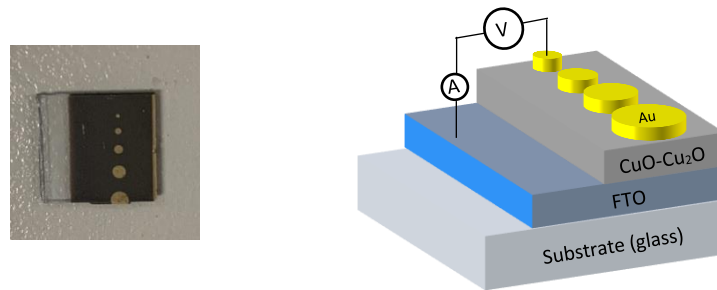
Figure 2.4. The FTO/CuO-Cu$_2$O/Au I-V characteristics.
(a) The schematic picture (left) and the structure of the fabricated devices (right).
(b) A typical RS behavior of the FTO/CuO-Cu$_2$O/Au device, where arrows indicate the RS operation cycle with ON and OFF switching
(c) The I-V characteristics at consecutive switching cycles

Cont. (b)
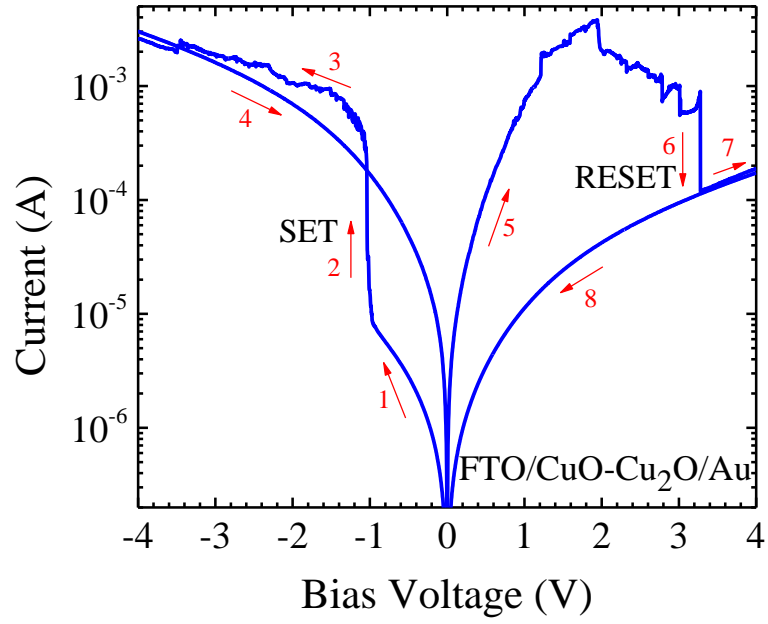
Cont. (c)
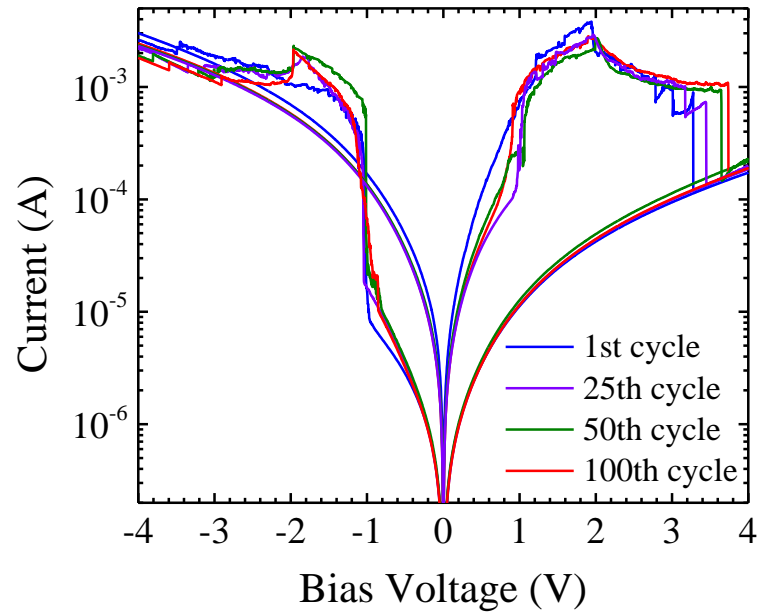
Figure 2.5(a) depicts the device endurance performance, in which the current values of LRS and HRS are monitored at 0.2 V. The HRS current state is consistent over 100 cycles, and LRS current also becomes stable after the first several cycles, indicating a good endurance of the device performance. From the current ratio, the memory window is maintained well at more than one order of magnitude difference thus, we can well distinguish between the binary storage information. The retention characteristic is shown in Figure 2.5(b), which demonstrate continuous sampling for around 2×10^4 s at room temperature. The HRS current state remains consistent while the LRS current decays a little bit after 10^3 s and again maintains consistency around 10 µA. The overall device performance is compared with recent publications in Table 1.

(a)
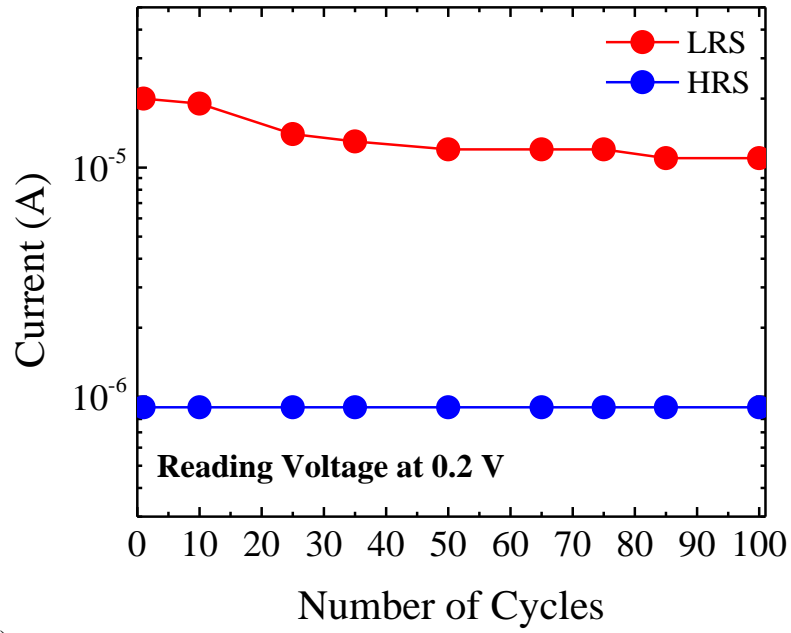
(b)
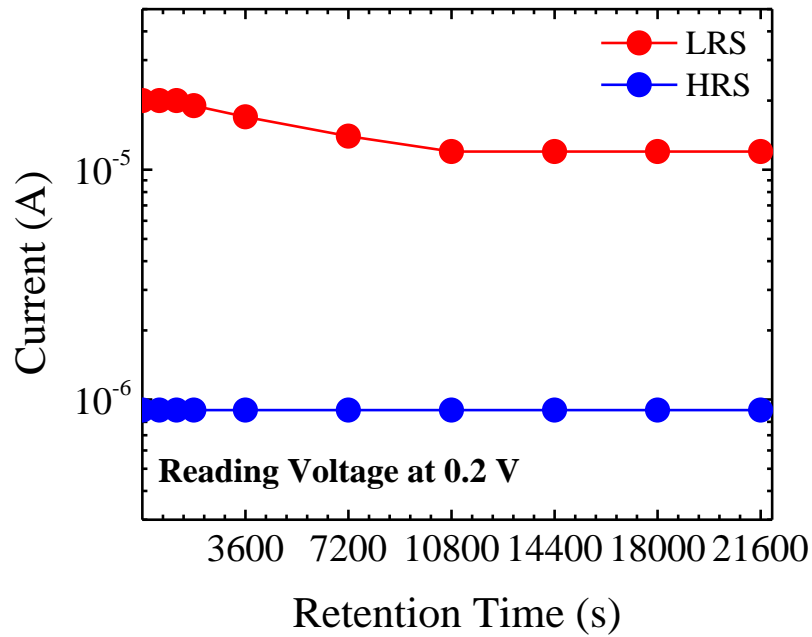
Figure 2.5. Endurance and retention stability performance of the device.
(a) Endurance performance of the device over 100 consecutive switching cycles.
(b) Retention performance of the device for around 2×10^4 s

Table 1: The device performance comparison between this work and
other publications regarding copper oxide resistive switching.

Device Structure	Endurance (cycle)	Retention (s)	Set/Reset (V)	Power Consumption (W)	On/Off Ratio	$V_{forming}$ (V)	Fabrication Technique	Refs.
FTO/CuO-Cu_2O/Au	>100	>2×10^4	-1/+3.2	<4×10^{-6}	>10	6	thermal annealing	This work
ITO/ Cu_xO/Au	200	>10^4	-0.7/+0.7	<10×10^{-6}	>10	free	solution processing	[13]
Al/CuO/SS	-	600	+1.8/-1.8	-	-	free	hydrothermal	[9]
Ti/Cu_xO/Pt	100	>10^2	+0.8/-1	6×10^{-4}	100	14.8	thermal annealing	[27]
Cu/CuO/AgO/Ag	-	-	-0.8/+0.8	4×10^{-3}	10	free	solution processing	[14]
Cu/CuO/Ag	100	-	+2/-2	-	-	free	thermal annealing	[12]
Ti/Cu_2O/Cu	-	-	+0.55/-0.3	20×10^{-6}	>10	free	DC sputtering	[34]

To further understand the switching and conduction mechanism of the device, the linear fitting I-V characteristics of positive and negative bias regions are plotted on a separate double logarithmic scale (Figure 2.6). In the low voltage negative bias region (Figure 2.6(a)), the curve's slope is approximately 1 for both HRS and LRS states, indicating the Ohmic conduction is dominant at low voltages ($I \propto V$). It means that thermally generated free carriers in the oxide film mainly contribute to the conduction and exceed injected carriers when the applied bias voltage is low. As the negative voltage scans forward, the curve's slope increases to 2, which is following Child's square law ($I \propto V^2$). In the higher field regions, a steep current increase occurs around 1 V due to the formation of filaments and trapping the injected carriers in the oxide layer where $I \propto V^a$ (a>2). For copper oxide thin films, the traps are well known to be as oxygen vacancies. When traps or oxygen vacancies are gradually filled by injected carriers, the slope reduces to around 2 again [30]. Therefore, the fitting results suggest that the conduction mechanism follows the space charge limited conduction (SCLC) model. This model is constituted of three regions: (1) Ohmic

region, (2) Child's square law or trap-unfilled SCLC region, and (3) trap-filled SCLC region. According to the SCLC theory at higher fields or trap-free SCLC region,

$$J = \frac{9}{8} \varepsilon \mu \theta \frac{V^2}{d^3}$$

Where J is the current density, ε is the permittivity of the oxide layer, μ is the mobility of charge carriers, θ is the ratio between free and shallow trapped charge carriers, and d is the film thickness [35]. In the positive bias region (Figure 2.6(b)), a similar conduction mechanism is observed, which obeys the SCLC model. The LRS state with a slope of 1 is still maintained, which is followed by the Child's law with a slope of 2 until the rupture of conductive filament gradually occurs, and the device resets back to HRS.

(a)
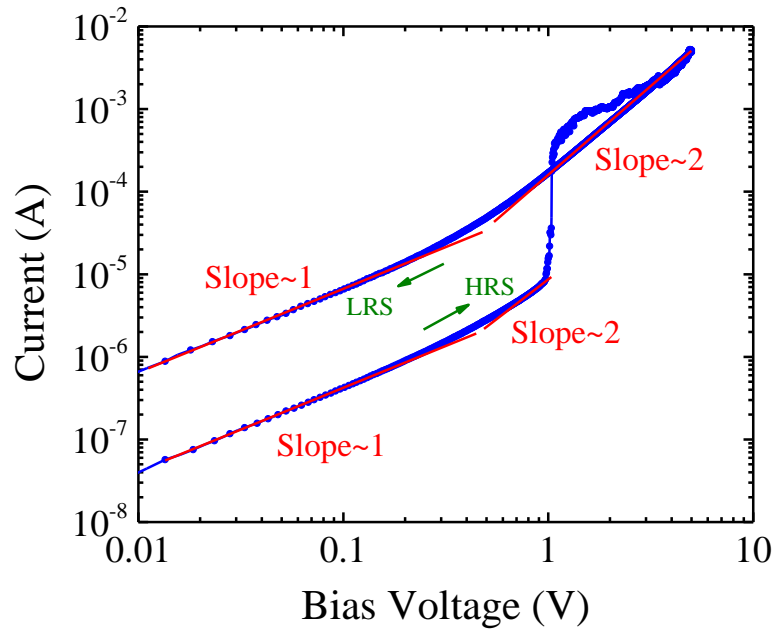
(b)
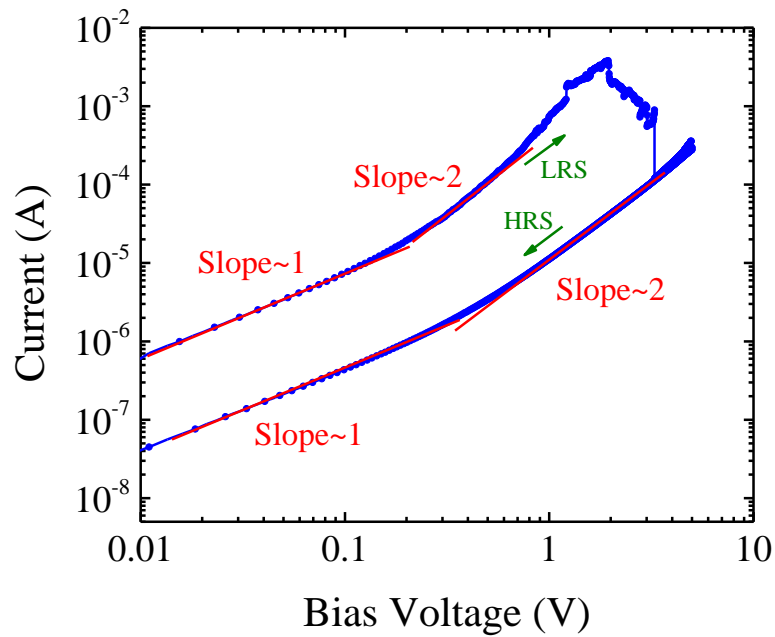
Figure 2.6. The linear fitting, I-V characteristics for the double logarithmic plots of Fig. 3b, indicating the corresponding curve's slopes and the conduction mechanism of the device.
(a) Negative voltage bias region
(b) Positive voltage bias region

Based on the above analysis, the RS mechanism is bipolar in which the SET and RESET processes occur in different polarities. The resistive switching mechanism in the device is shown in Figure 2.7. The forming or SET process is due to a dielectric soft breakdown in the oxide layer [36], and then oxygen ions (O^{2-}) move through the filament (oxygen vacancies) to the anode as an oxygen vacancy absorber (FTO). At the anode interface, the oxygen ions reoxidize ($O^{2-} = O + 2e^-$), creating an oxygen reservoir [29]. The RESET process occurs at the reverse polarity where oxygen ions are repelled from the anode interface because they are negatively charged. Therefore, based on the external voltage polarity, the oxygen ions are repelled or extracted back to the anode, switching the device between LRS and HRS states. A detailed explanation of the filamentary switching mechanism remains an area of active research.

$$O^{2-} \leftrightarrow O_2 + 2e^-$$
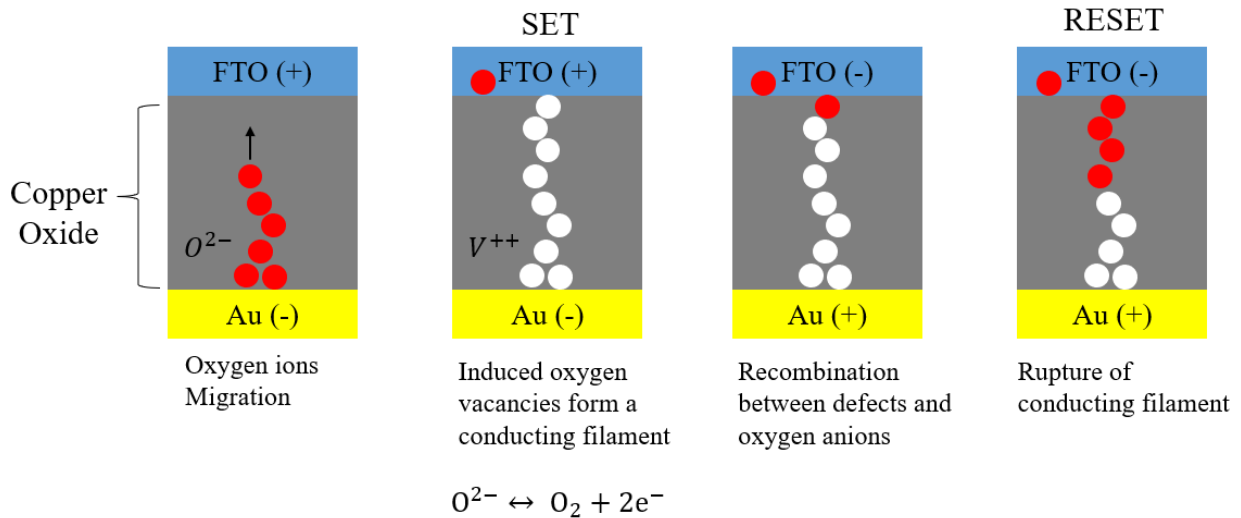
Figure 2.7. The resistive switching mechanism in the copper oxide layer.

Conclusion

In summary, we reported a facile fabrication method and analyzed the resistive switching behavior of the heterogenous electrodes structure of FTO/CuO-Cu2O/Au memristor. The copper oxide complex layer after annealing is investigated by Raman and absorbance measurements. The

conduction mechanism of this device is also investigated, which follows the space charge limited conduction (SCLC) theory. The achieved results suggest high endurance, low SET voltage, and efficient power consumption of the device. However, further investigations are required to increase the retention time and on/off ratio in this type of memristor.

Acknowledgments

References

[1] L. Chua, "Memristor-The missing circuit element," *IEEE Trans. Circuit Theory*, vol. 18, no. 5, pp. 507–519, 1971, doi: 10.1109/TCT.1971.1083337.

[2] W. Sun *et al.*, "Understanding memristive switching via in situ characterization and device modeling," *Nat. Commun.*, vol. 10, no. 1, p. 3453, Dec. 2019, doi: 10.1038/s41467-019-11411-6.

[3] D. B. Strukov, G. S. Snider, D. R. Stewart, and R. S. Williams, "The missing memristor found," *Nature*, vol. 453, no. 7191, pp. 80–83, May 2008, doi: 10.1038/nature06932.

[4] G. Niu *et al.*, "Geometric conductive filament confinement by nanotips for resistive switching of HfO2-RRAM devices with high performance," *Sci. Rep.*, vol. 6, no. 1, p. 25757, Sep. 2016, doi: 10.1038/srep25757.

[5] M. Laurenti, S. Porro, C. F. Pirri, C. Ricciardi, and A. Chiolerio, "Zinc Oxide Thin Films for Memristive Devices: A Review," *Crit. Rev. Solid State Mater. Sci.*, vol. 42, no. 2, pp. 153–172, Mar. 2017, doi: 10.1080/10408436.2016.1192988.

[6] C. Liu *et al.*, "Synaptic functions and a memristive mechanism on Pt/AlO$_x$/HfO$_x$/TiN bilayer-structure memristors," *J. Phys. Appl. Phys.*, vol. 53, no. 3, p. 035302, Jan. 2020, doi: 10.1088/1361-6463/ab4e70.

[7] Q. Xia and J. J. Yang, "Memristive crossbar arrays for brain-inspired computing," *Nat. Mater.*, vol. 18, no. 4, pp. 309–323, Apr. 2019, doi: 10.1038/s41563-019-0291-x.

[8] W. Kim, A. Chattopadhyay, A. Siemon, E. Linn, R. Waser, and V. Rana, "Multistate Memristive Tantalum Oxide Devices for Ternary Arithmetic," *Sci. Rep.*, vol. 6, no. 1, p. 36652, Dec. 2016, doi: 10.1038/srep36652.

[9] T. D. Dongale *et al.*, "Mimicking the Synaptic Weights and Human Forgetting Curve Using Hydrothermally Grown Nanostructured CuO Memristor Device," *J. Nanosci. Nanotechnol.*, vol. 18, no. 2, pp. 984–991, Feb. 2018, doi: 10.1166/jnn.2018.14264.

[10] C. Nyenke and L. Dong, "Fabrication of a W/CuxO/Cu memristor with sub-micron holes for passive sensing of oxygen," *Microelectron. Eng.*, vol. 164, pp. 48–52, Oct. 2016, doi: 10.1016/j.mee.2016.07.005.

[11] H. Liu, Y. Liu, W. Guo, X. Zhou, L. Lin, and P. Peng, "Laser assisted ink-printing of copper oxide nanoplates for memory device," *Mater. Lett.*, vol. 261, p. 127097, Feb. 2020, doi: 10.1016/j.matlet.2019.127097.

[12] L. Ortega-Reyes and A. Ávila-García, "Memristors based on thermal copper oxide," *J. Mater. Sci. Mater. Electron.*, Jan. 2020, doi: 10.1007/s10854-020-02963-1.

[13] S. Rehman, J.-H. Hur, and D. Kim, "Resistive Switching in Solution-Processed Copper Oxide (Cu $_x$ O) by Stoichiometry Tuning," *J. Phys. Chem. C*, vol. 122, no. 20, pp. 11076–11085, May 2018, doi: 10.1021/acs.jpcc.8b00432.

[14] P. Xu, M. C. Hamilton, and S. Zou, "Resistive switching characteristics in printed Cu/CuO/(AgO)/Ag memristors," *Electron. Lett.*, vol. 49, no. 13, pp. 829–830, Jun. 2013, doi: 10.1049/el.2013.1302.

[15] Y. Li, S. Long, Q. Liu, H. Lv, and M. Liu, "Resistive Switching Performance Improvement via Modulating Nanoscale Conductive Filament, Involving the Application of Two-Dimensional Layered Materials," *Small*, vol. 13, no. 35, p. 1604306, Sep. 2017, doi: 10.1002/smll.201604306.

[16] C. Sung, H. Hwang, and I. K. Yoo, "Perspective: A review on memristive hardware for neuromorphic computation," *J. Appl. Phys.*, vol. 124, no. 15, p. 151903, Oct. 2018, doi: 10.1063/1.5037835.

[17] T. Shi, X.-B. Yin, R. Yang, and X. Guo, "Pt/WO $_3$ /FTO memristive devices with recoverable pseudo-electroforming for time-delay switches in neuromorphic computing," *Phys. Chem. Chem. Phys.*, vol. 18, no. 14, pp. 9338–9343, 2016, doi: 10.1039/C5CP07675G.

[18] J. K. Yang, B. Liang, M. J. Zhao, Y. Gao, F. C. Zhang, and H. L. Zhao, "Reference of Temperature and Time during tempering process for non-stoichiometric FTO films," *Sci. Rep.*, vol. 5, no. 1, p. 15001, Dec. 2015, doi: 10.1038/srep15001.

[19] Y. Khrapovitskaya, N. Maslova, I. Sokolov, Y. Grishchenko, D. Mamichev, and M. Zanaveskin, "The titanium oxide memristor contact material's influence on element's cyclic stability to degradation: The titanium oxide memristor contact material's influence on element's cyclic stability to degradation," *Phys. Status Solidi C*, vol. 12, no. 1–2, pp. 202–205, Jan. 2015, doi: 10.1002/pssc.201400109.

[20] L.-C. Chen *et al.*, "Nano-structured CuO-Cu2O Complex Thin Film for Application in CH3NH3PbI3 Perovskite Solar Cells," *Nanoscale Res. Lett.*, vol. 11, no. 1, p. 402, Dec. 2016, doi: 10.1186/s11671-016-1621-4.

[21] N. R. Dhineshbabu, V. Rajendran, N. Nithyavathy, and R. Vetumperumal, "Study of structural and optical properties of cupric oxide nanoparticles," *Appl. Nanosci.*, vol. 6, no. 6, pp. 933–939, Aug. 2016, doi: 10.1007/s13204-015-0499-2.

[22] O. Madelung, *Semiconductors: Data Handbook.* Springer Science & Business Media, 2012.

[23] F. A. Akgul, G. Akgul, N. Yildirim, H. E. Unalan, and R. Turan, "Influence of thermal annealing on microstructural, morphological, optical properties and surface electronic structure of copper oxide thin films," *Mater. Chem. Phys.*, vol. 147, no. 3, pp. 987–995, Oct. 2014, doi: 10.1016/j.matchemphys.2014.06.047.

[24] K. S. Wanjala, W. K. Njoroge, N. E. Makori, and J. M. Ngaruiya, "Optical and Electrical Characterization of CuO Thin Films as Absorber Material for Solar Cell Applications," *Am. J. Condens. Matter Phys.*, vol. 6, no. 1, pp. 1–6, 2016.

[25] W. Zheng, Y. Chen, X. Peng, K. Zhong, Y. Lin, and Z. Huang, "The Phase Evolution and Physical Properties of Binary Copper Oxide Thin Films Prepared by Reactive Magnetron Sputtering," *Mater. Basel Switz.*, vol. 11, no. 7, Jul. 2018, doi: 10.3390/ma11071253.

[26] T. Wang *et al.*, "Electroforming in Metal-Oxide Memristive Synapses," *ACS Appl. Mater. Interfaces*, vol. 12, no. 10, pp. 11806–11814, Mar. 2020, doi: 10.1021/acsami.9b19362.

[27] S.-Y. Wang, C.-W. Huang, D.-Y. Lee, T.-Y. Tseng, and T.-C. Chang, "Multilevel resistive switching in Ti/CuxO/Pt memory devices," *J. Appl. Phys.*, vol. 108, no. 11, p. 114110, Dec. 2010, doi: 10.1063/1.3518514.

[28] J.-J. Huang, C.-W. Kuo, W.-C. Chang, and T.-H. Hou, "Transition of stable rectification to resistive-switching in Ti/TiO2/Pt oxide diode," *Appl. Phys. Lett.*, vol. 96, no. 26, p. 262901, Jun. 2010, doi: 10.1063/1.3457866.

[29] H.-S. P. Wong *et al.*, "Metal–Oxide RRAM," *Proc. IEEE*, vol. 100, no. 6, pp. 1951–1970, Jun. 2012, doi: 10.1109/JPROC.2012.2190369.

[30] Y. B. Zhu, K. Zheng, X. Wu, and L. K. Ang, "Enhanced stability of filament-type resistive switching by interface engineering," *Sci. Rep.*, vol. 7, no. 1, p. 43664, May 2017, doi: 10.1038/srep43664.

[31] K.-H. Chen *et al.*, "Effect of different constant compliance current for hopping conduction distance properties of the Sn:SiOx thin film RRAM devices," *Appl. Phys. A*, vol. 122, no. 3, p. 228, Mar. 2016, doi: 10.1007/s00339-016-9768-5.

[32] Y. C. Yang, F. Pan, Q. Liu, M. Liu, and F. Zeng, "Fully Room-Temperature-Fabricated Nonvolatile Resistive Memory for Ultrafast and High-Density Memory Application," *Nano Lett.*, vol. 9, no. 4, pp. 1636–1643, Apr. 2009, doi: 10.1021/nl900006g.

[33] Y.-S. Fan and P.-T. Liu, "Characteristic Evolution From Rectifier Schottky Diode to Resistive-Switching Memory With Al-Doped Zinc Tin Oxide Film," *IEEE Trans. Electron Devices*, vol. 61, no. 4, pp. 1071–1076, Apr. 2014, doi: 10.1109/TED.2014.2305155.

[34] P. Yan *et al.*, "Conducting mechanisms of forming-free TiW/Cu $_2$ O/Cu memristive devices," *Appl. Phys. Lett.*, vol. 107, no. 8, p. 083501, Aug. 2015, doi: 10.1063/1.4928979.

[35] M. A. Lampert and R. B. Schilling, "Chapter 1 Current Injection in Solids: The Regional Approximation Method," in *Semiconductors and Semimetals*, vol. 6, Elsevier, 1970, pp. 1–96. doi: 10.1016/S0080-8784(08)62630-7.

[36] N. Xu *et al.*, "Characteristics and mechanism of conduction/set process in TiN∕ZnO∕Pt resistance switching random-access memories," *Appl. Phys. Lett.*, vol. 92, no. 23, p. 232112, Jun. 2008, doi: 10.1063/1.2945278.

Chapter 3: Effects of high temperature annealing on the performance of copper oxide photodetectors

Abstract

Copper oxide thin films are grown using copper nanofilms oxidized at high annealing temperatures. The thin film crystallinity and surface morphology are probed using the X-ray diffractometer and scanning electron microscopy, indicating that the crystalline quality of the copper oxide thin films is improved by increasing the annealing temperature. Under ultraviolet-visible light illumination, the fabricated device with thin films annealed at 900 °C and the corresponding bandgap of 2.8 eV demonstrates the high responsivity of 15.1 A/W and maximum detectivity of 4.52×10^{12} cmHz$^{1/2}$/W. The photosensitivity of thin films annealed at 900 °C is more than ten times higher than that of thin films annealed at 800 °C. The fabricated device works as a visible-ultraviolet photodetector and maintains uniform and stable performance for a tested period of eight weeks.

Introduction

According to recent studies, high-performance photodetectors are fabricated based on various materials including metal oxides[1], perovskites[2,3], and transition metal dichalcogenides[4,5]. Light-sensitive materials are synthesized in different forms and dimensions, like thin films, quantum dots, nanowires, and two-dimensional materials[6]. Among different materials, copper oxide is one of the most important metal oxide p-type semiconductors, which is widely used in various optoelectronic applications, such as photodetectors[7], solar cells[8], and memristors[9]. A facile fabrication process and the stabilized characteristics of copper oxide thin films make them

suitable materials for ultraviolet[10] and visible-light photodetectors[11]. Moreover, there is a possibility to effectively tune the bandgap of copper oxide compounds and significantly enhance the corresponding optical absorption[12]. Therefore, copper oxide-based photodetectors can be an alternative to other high-performance photodetectors. However, the research on copper oxide photodetectors is still at an early stage, and rigorous studies on the device optoelectronic characteristics are required to enhance the photodetector performance in terms of photosensitivity, detectivity, and responsivity[13].

Various methods are used to prepare copper oxide thin films, such as magnetron sputtering, sol-gel, pyrolysis, hydrothermal, pulsed laser deposition, thermal oxidation, and chemical vapor deposition. Among these growth methods, thermal annealing is considered a facile and fast fabrication method to grow copper oxide thin films and nanowires. In this method, the copper thin films are simply subjected to heat treatments at high temperatures. The thin film's crystallinity and surface morphology can be modified by controlling the heating rates, oxidation percentage, and pressure[14]. Recently, a visible-light photodetector based on copper oxide thin films is investigated using a grain-structure model[15], which suggests the thermal annealing method to grow copper oxide thin films for high-performance visible-light photodetectors. Another interesting application of the thermal annealing method is in the growth of copper oxide nanowires, which has attracted considerable attention due to its high sensitivity and stability for gas sensing applications. The work reported by Steinhauer[16], describes local CuO nanowires growth on microplates and integration into a conductometric gas sensing device.

In this work, we report on the effect of high annealing temperature on the surface morphology of copper oxide thin films to develop a UV-Visible photodetector. First, the deposited copper thin films are annealed in air at temperatures of 800 °C, 850 °C, and 900 °C using the

conventional thermal annealing method. Then, the crystallinity and surface morphology of the copper oxide thin films are investigated to understand the effect of annealing temperature and heating rate on the copper oxide optical properties. As a result, by controlling the annealing temperature, the grain size and surface morphologies of the copper oxide thin films can be engineered. Several photodetectors using prepared copper oxide thin films are fabricated, and the current-voltage characteristics, photosensitivity, detectivity, and stability are investigated using light sources with different intensities. The optoelectronic performance of the photodetector is optimized simply by adjusting the annealing temperature of the copper oxide thin films. Finally, the stable and reliable performance of the fabricated copper oxide photodetector illuminated by the low-intensity light is confirmed.
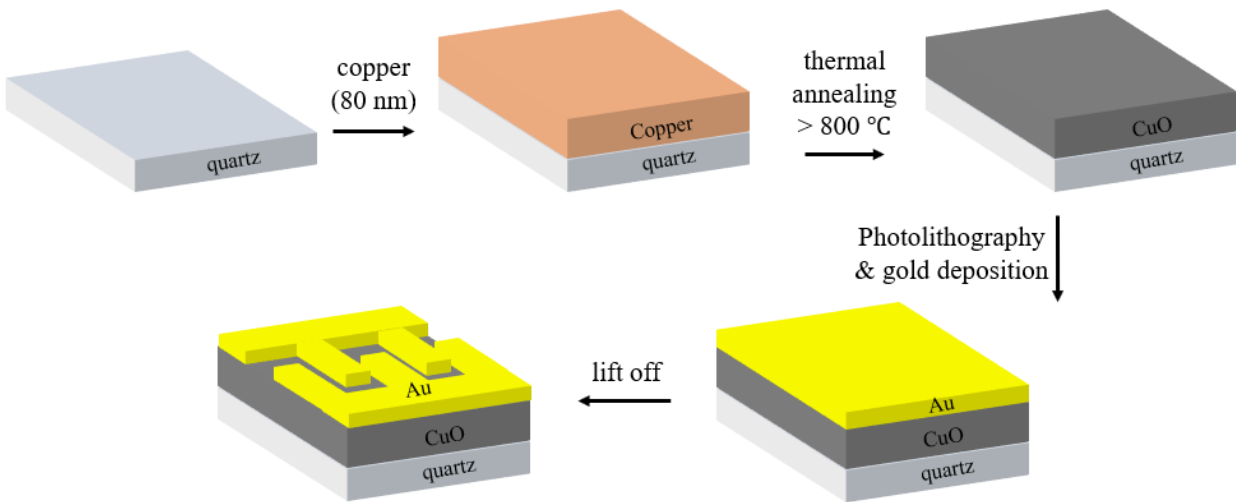

Figure 3.1. The fabrication process of copper oxide photodetectors.

Experimental

The quartz substrates were rinsed ultrasonically using isopropanol, acetone, methanol, and deionized water. The 80 nm-thick copper (Cu) thin films were deposited on the quartz substrate

using Angstrom Nexdep electron-beam evaporator at room temperature. The vacuum pressure was kept at 6×10^{-7} Torr during the deposition process. The as-deposited Cu thin films were annealed at 800, 850, and 900 °C for 1h in an oxygen ambient environment with a heating rate of 25 °C/min and natural cooling to form the copper oxide thin films using the Thermo Scientific muffle furnace. The fabrication process of the device is shown in Figure 3.1. We used Philips PW1830 X-ray Diffractometer (XRD) and Cary 500 UV-Vis-NIR Spectrophotometer to characterize the XRD and absorbance properties of the thin films, respectively. The absorbance of the grown thin films was measured in the wavelength range of 200 – 800 nm, where the excitonic peak and bandgap of the copper oxide can be observed. To achieve Au/CuO/Au devices, the 50 nm-thick interdigital gold (Au) electrodes with the 10 µm finger-spacing were deposited using the photolithography method following by the electron beam evaporation and lift-off process. The fabrication process is facile and straightforward without any adhesion problems of copper oxide annealed at high temperatures. We used a solar simulator as a light source with similar spectral composition to the sunlight from UV to near-infrared and Keithley 4200 SCS parameter analyzer is utilized for the current-voltage (I-V) characterization of the fabricated devices. All the measurements were performed at room temperature.

Results and discussion

Figure 3.2(a) plots the XRD results of the prepared copper oxide thin films. The strong peaks at 35.6º [002], 38.8º [111], and a weak peak at 32.6º [110] are all ascribed to the cupric oxide (CuO) phase. The sharp diffraction peaks indicate the formation of CuO monoclinic crystal phase. The corresponding 2θ of the characteristic diffraction peaks of the three samples are consistent, indicating that all the samples have the same phase. The dominant peaks at 35.6º [002] and 38.8º [111] are increasing by the annealing temperature, indicating that the crystalline quality of the CuO

thin films is improved by increasing the annealing temperature. Likewise, the optical absorption of CuO thin films is shown in Figure 3.2(b). The absorption peak shifts from the UV to the visible region by increasing the annealing temperature, which might be due to the change in the copper oxide surface morphology[17]. The thin films annealed at 900 ºC exhibits high absorbance in the visible region centered around 450 nm. Figure 3.2(c) demonstrates the 80 nm-thick copper oxide thin films deposited on the quartz substrate and the corresponding SEM images of thin films annealed at different temperatures are shown in Figure 3.2(d). The grain size is increasing, and the grain boundaries are decreasing as the temperature is elevated to 900 ºC. As a result, the surface morphology of the copper oxide thin films is largely influenced by temperature, as indicated by SEM images and XRD spectroscopy. With an increase in annealing temperature, the average size of cubic-shape grains increased, and thin-films crystallinity improved. The absorption peak shifts from the UV to the Visible region by increasing the annealing temperature, and the energy bandgap slightly shifts. The absorption spectrum is used to achieve Tauc plot from which the bandgap of CuO is determined. The corresponding copper oxide phase is a cupric oxide (CuO) which is a dominant phase in high annealing temperature. These thin films are used to fabricate interdigital photodetectors with the finger-spacing of 10 µm.
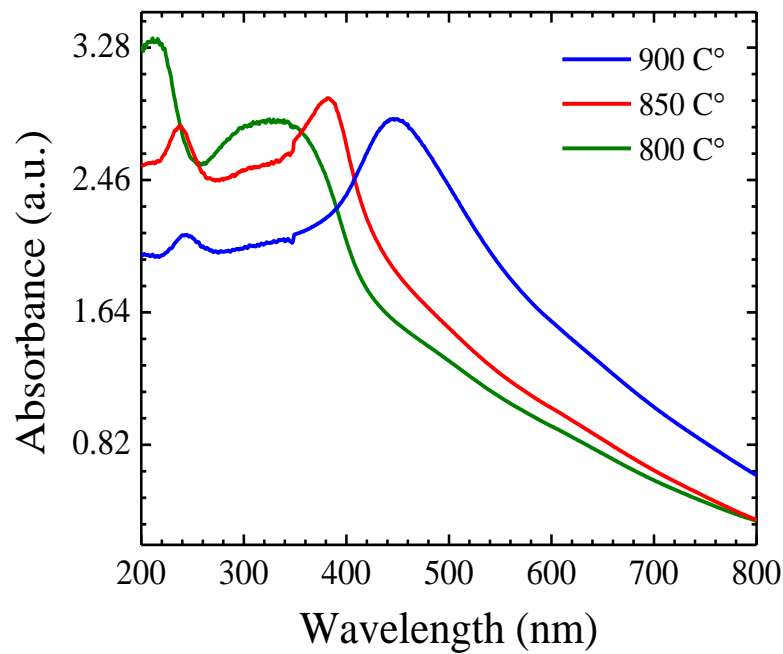
(a)
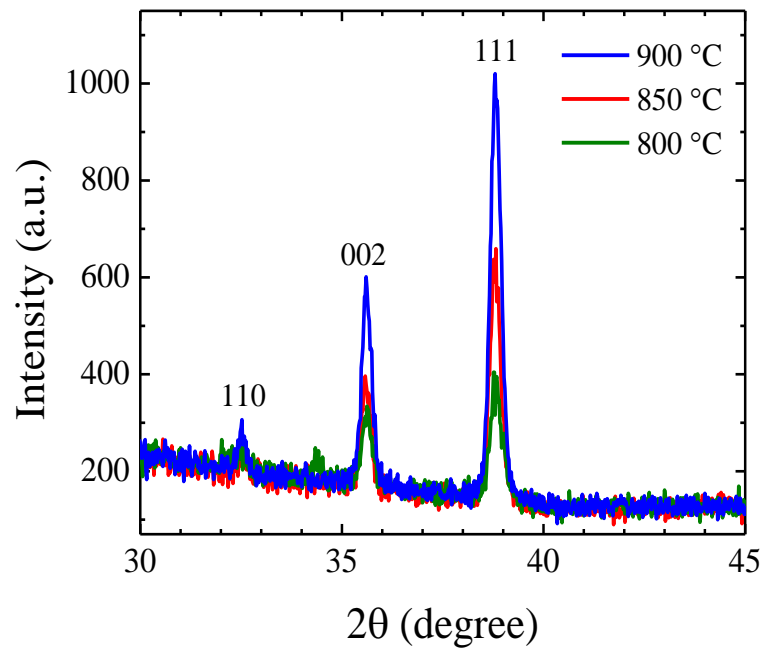
(b)

Figure 3.2. (a) XRD patterns of the copper oxide thin films are shown at different annealing temperatures. (b) The absorbance spectra of the copper oxide thin films are shown at different annealing temperatures. (c) The 80 nm-thick copper oxide thin films on the quartz substrate. (d) The corresponding SEM images taken from samples annealed at different temperatures.

Cont.

(c)

(d)

Annealed at 800 ℃   Annealed at 850 ℃   Annealed at 900 ℃

2 µm   2 µm   2 µm
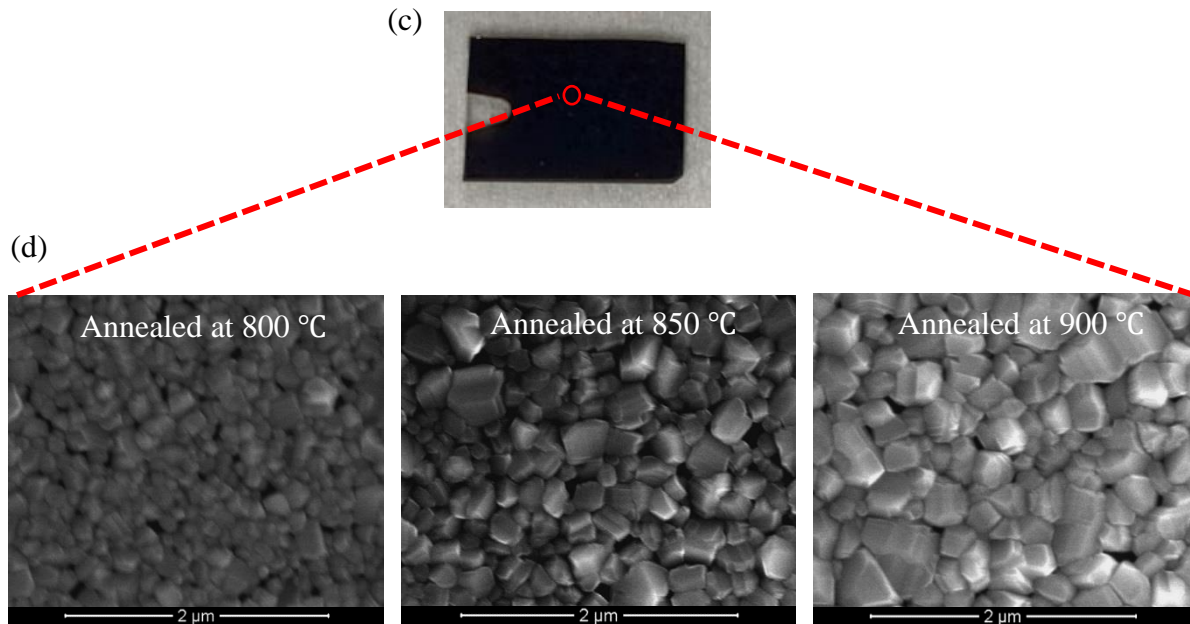
The current-voltage (I-V) characterization of the fabricated photodetectors is measured at room temperature under different light intensities. Figure 3.3(a) shows the I-V characteristics of the devices based on copper thin films annealed at temperatures of 800, 850, and 900 ℃. The I-V characteristic is asymmetric, suggesting the Au-CuO junction is Schottky. The dark current is strongly affected by increasing the annealing temperature to 900 ℃, which can be explained by the grain-structure model. The copper oxide grain size significantly increases by increasing the annealing temperature, reducing the contacting size between adjacent grains. Therefore, the dark current decreases because the contact resistance increases. likewise, the photocurrent is also increasing by the annealing temperature since the generation of photocarriers increases by the larger grain size[18]. The devices annealed at 800 °C experience a less significant drop in the dark current or increase in the photocurrent because of the smaller grain sizes and the corresponding absorbance peak is in the UV range. Figure 3.3(b) demonstrates multiple photo-switching cycles of different devices at a bias voltage of 5 V. The rise time is higher than the decay time because of

the slow surface oxygen adsorption. Under light illumination, the electron-hole pairs are generated in the copper oxide thin films, leading to an increase in photocurrent. Besides, photo-generated electrons also react with oxygen at the surface before electrons recombined with unpaired holes, resulting in the slow increase of the photocurrent. Without light illumination, at first, the photocurrent drops abruptly due to the photocarriers recombination following by a slow decay because of the reaction of remaining holes and oxygen ions. Figure 3.3(c) shows the photosensitivity or I_{light}/I_{dark} ratio, which is increasing with the light intensity. The fabricated device using copper thin films annealed at 900 °C shows enhanced photosensitivity compared to other devices because of higher photocurrent and lower dark current. The interdigital device with the finger-spacing of 10 µm and gold electrodes is depicted in Figure 3.3(d).

(a)
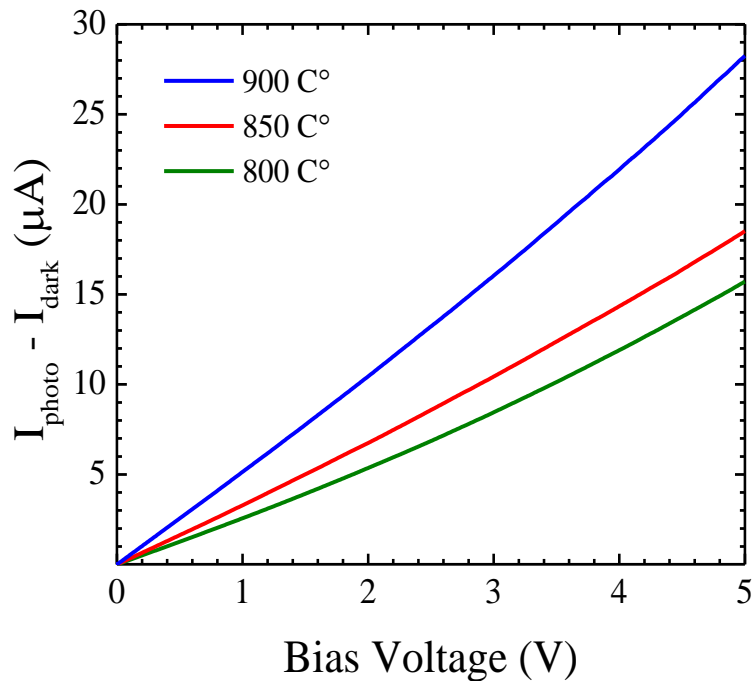
Figure 3.3. (a) I-V characteristics of the copper oxide photodetectors are demonstrated with the thin films annealed at 800, 850, and 900 ℃. (b) Time-resolved currents of copper oxide photodetectors are shown with the thin films annealed at 800, 850, and 900 ℃ measured under multiple on/off illumination cycles at a bias voltage of 5 V (light intensity: 100 mW/cm^2. (c) Photosensitivity (On/Off ratio) of a photodetector fabricated at 800 ℃, 850 ℃, and 900 ℃

annealing temperature as a function of optical light intensity measured at a bias voltage of 5 V. (d) Photograph of the fabricated photodetector annealed at 900 ℃ (left) and the magnified image of the interdigital structure (right).

Cont. (b)

Cont. (c)

Cont. (d)

Electrode (Au) (Au)

CuO (p-type)

(bandgap~ 2.8 eV)
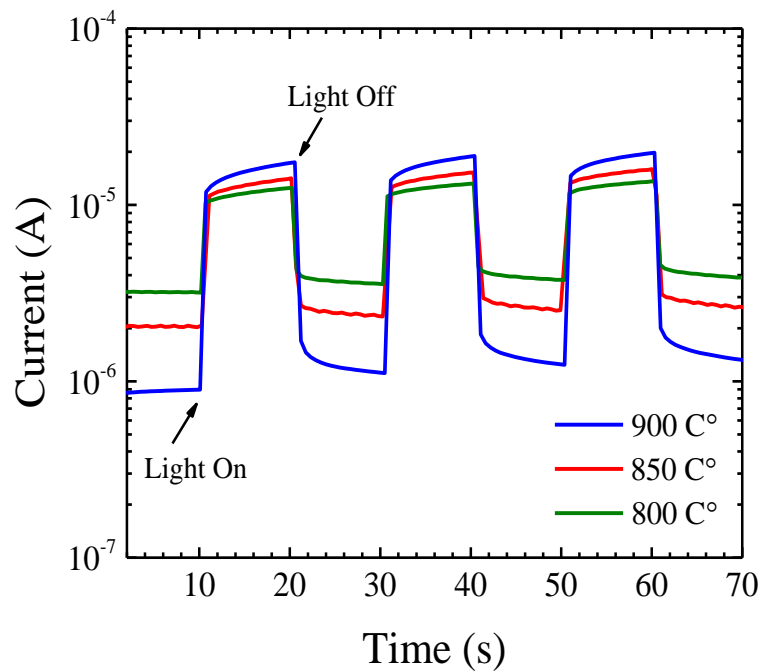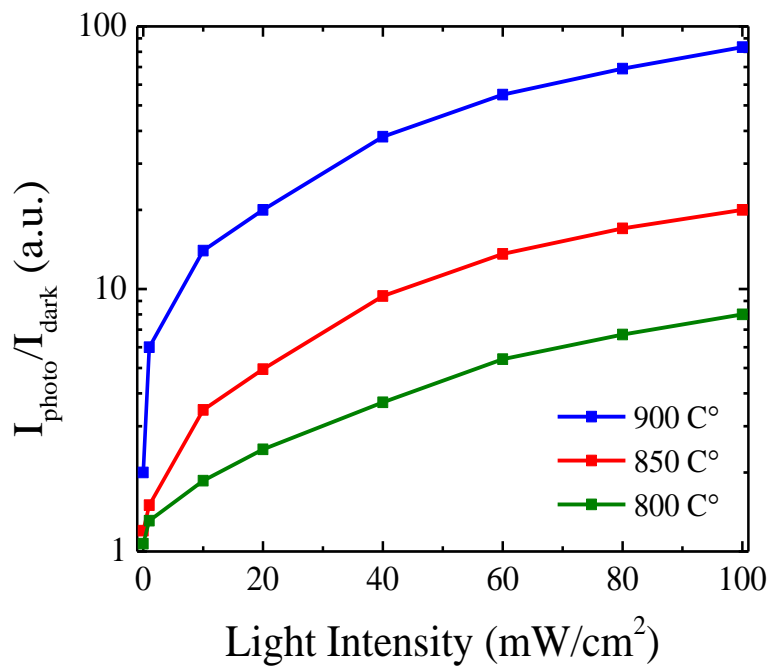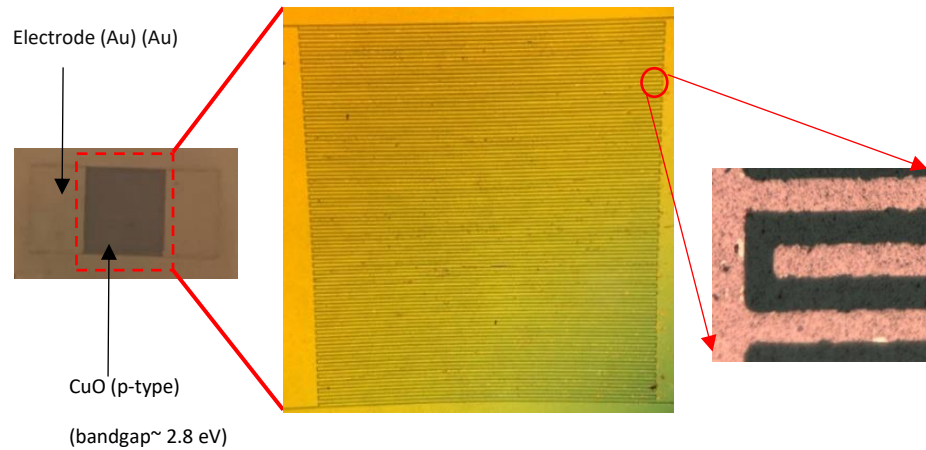
The detectivity and responsivity of the devices annealed at differ ent temperatures as a function of the light intensity at the bias voltage of 5 V are shown in Figure 3.4(a). The device which is fabricated at the annealing temperature of 900 °C exhibits the highest detectivity and responsivity compared to those annealed at 850 °C and 800 °C. The responsivity is given by $R = I_{photo}/P_{in}$ (A/W), and detectivity is given by $D^* = R/(2eI_{dark}/S)^{1/2}$ (cm.Hz$^{1/2}$/W), where P_{in} is the incident light intensity, and S is the surface area of the device[19]. Responsivity is the measure of photocurrent per optical input and Detectivity is a figure of merit to determine the ability of a photodetector to detect weak signals. Both responsivity and detectivity are decreasing by increasing the light intensity because of the high carrier concentration and recombination of excitons[16]. The highest responsivity of 15.1 A/W is achieved for a device annealed at 900 °C under the light intensity of 10 µW, and the corresponding detectivity is 4.52×10^{12} cm.Hz$^{1/2}$/W. Figure 3.4(b) illustrates the reliability performance of the device tested for a specific time. The fabricated device using copper thin films annealed at 900 °C maintains its detectivity and responsivity without significant degradation for over eight weeks, which implies that the copper oxide-based photodetector has a strong potential for practical applications and can be used as a UV-Visible photodetector.

(a)
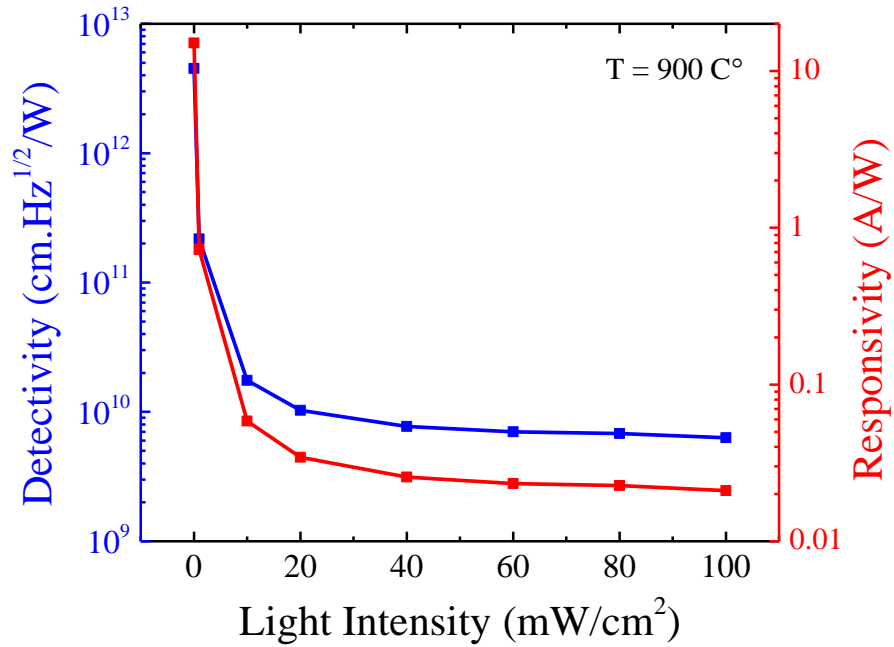
(b)

Figure 3.4. (a) Detectivity and responsivity of a photodetector fabricated at 900 ℃ annealing temperature as a function of optical light intensity is measured at a bias voltage of 5 V. (b) Detectivity and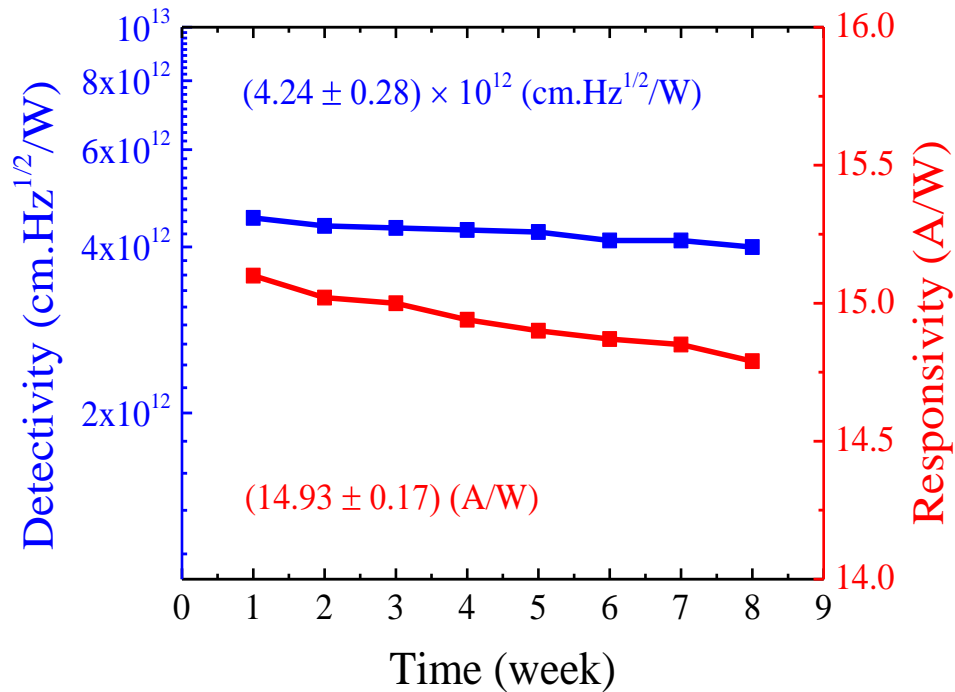 responsivity performance over eight weeks of operation is shown. The device is fabricated at 900 ℃ annealing temperature and measured at a bias voltage of 5 V.

Table I. Comparison of this work with copper oxide-based photodetectors in literature.

Materials	I_{on}/I_{off}	R (A/W)	D^* (Jones)	SR (nm)	Ref.
CuO	1.04	15.3	1.08×10^{11}	400-700	(18)
CuO	610	14.02	3.59×10^{13}	210-290	(10)
SnO_2/CuO	592	10.3	-	280	(20)
CuO	57.5	0.59	4.6×10^{8}	620-750	(11)
PVK/Cu_2O	-	10.23	3.0×10^{11}	632	(21)
CuO/ZnO	-	8.74	4.5×10^{10}	405	(22)
CuO	87	15.1	4.52×10^{12}	365-800	This work

The important device characteristics of this work are compared with previously reported copper oxide-based photodetectors in Table I.

Conclusion

In summary, we developed a UV-Visible copper oxide-based thin films photodetector, which demonstrates enhanced optoelectronic performances when the device is fabricated at higher annealing temperatures. The surface morphology of copper oxide thin films is engineered by thermal annealing to cover UV-Visible spectral range. We explained the results by the grain-structure model and the effects of the large grain size on the dark current, photocurrent, photosensitivity, responsivity and detectivity are investigated. We confirmed that the fabricated device is reliable by testing the detectivity performance for over eight weeks. Therefore, the results reveal that the fabricated copper oxide photodetector is reliable and can be considered in practical optoelectronic applications.

Acknowledgments

References

1) M. Patel, H-S. Kim, J. Kim, Adv Electron Mater. **1**, 1500232 (2015).

2) J. Miao, F. Zhang, J Mater Chem C. **7**, 1741 (2019).

3) H. Salman, A. Shariffar, T. A. Siddique, M. O. Manasreh, MRS Adv. **5**, 2537 (2020).

4) S. Manzeli, D. Ovchinnikov, D. Pasquier, O. V. Yazyev, A. Kis, Nat Rev Mater. **2**, 17033 (2017).

5) H. Lee, J. Ahn, S. Im, J. Kim, W. Choi, Sci Rep. **8**, 11545 (2018).

6) S. M. Sze, *Physics of Semiconductor Devices* (Wiley, New York, 1981) 2nd ed., p. 55.

7) S. Lee, W-Y. Lee, B. Jang, T. Kim, J-H. Bae, K. Cho, IEEE Electron Device Lett. **39**, 47 (2018).

8) T. Wong, S. Zhuk, S. Masudy-Panah, G. Dalapati, Materials. **9**, 271 (2016).

9) A. Shariffar, H. Salman, T. A. Siddique, W. Gebril, M. O. Manasreh, Micro Nano Lett. **15**, 853 (2020).

10) T. Dixit, A. Tripathi, S. V. Solanke, K. L. Ganapathi, M. S. R. Rao, V. Singh, IEEE Electron Device Lett. **41**, 1790 (2020).

11) P. V. Raghavendra, J. S. Bhat, N. G. Deshpande, Superlattices Microstruct. **113**, 754 (2018).

12) S. Choudhary, J. V. N. Sarma, S. Pande, S. Ababou-Girard, P. Turban, B. Lepine, AIP Adv. **8**, 055114 (2018).

13) A. Bhaumik, A. M. Shearin, R. Patel, K. Ghosh, Chem Phys. **16**, 11054 (2014).

14) P. Sawicka-Chudy, M. Sibiński, E. Rybak-Wilusz, M. Cholewa, G. Wisz, R. Yavorskyi, AIP Adv. **10**, 010701 (2020).

15) G. Fritz-Popovski, F. Sosada-Ludwikowska, A. Köck, J. Keckes, G. A. Maier, Sci Rep. **9**, 807 (2019).

16) S. Steinhauer, A. Chapelle, P. Menini, M. Sowwan, ACS Sens. **1**, 503 (2016).

17) A. D. Faisal, W. K. Khalef, J Mater Sci Mater Electron. **28**, 18903 (2017).

18) H-J. Song, M-H. Seo, K-W. Choi, M-S. Jo, J-Y. Yoo, J-B. Yoon, Sci Rep. **9**, 7334 (2019).

19) C. Ma, Y. Shi, W. Hu, M. Chiu, Z. Liu, A. Bera, Adv Mater. **28**, 3683 (2016).

20) T. Xie, M. R. Hasan, B. Qiu, E. S. Arinze, N. V. Nguyen, A. Motayed, Appl Phys Lett. **107**, 241108 (2015).

21) Y-J. Chen, M-H. Li, J-Y. Liu, C-W. Chong, J-C-A. Huang, P. Chen, Opt Express. **27**, 24900 (2019).

22) A. Costas, C. Florica, N. Preda, A. Kuncser, I. Enculescu, Sci Rep. **10**, 18690 (2020).

Chapter 4: Effects of light illumination and the filaments confinement on the performance of CsPbBr₃ memory resistors

A. Shariffar, H. Salman, and M. O. Manasreh, "Effects of light illumination and the filaments confinement on the performance of CsPbBr₃ memory resistors,"

Abstract

Memristors are promising candidates for applications such as the internet of things and neuromorphic computing. To this aim, multifunctional memristors with low energy consumption, high stability, and retention time are required. The emerging optoelectronic memristors have the advantage of combining photonics and electronics into a multifunctional device. This study investigates the effects of light illumination on the resistive switching behavior of inorganic perovskite CsPbBr3-based memristor. First, A CsPbBr₃-based photodetector is fabricated and characterized which shows excellent photosensitivity. Second, the CsPbBr₃ thin film is used to fabricate a device with a gold-coated probe tip as the top electrode to confine the conductive filaments growth in CsPbBr₃ thin films. The obtained results demonstrate significant improvement in the resistive switching behavior in terms of stability and uniformity. The memconductance of this device can be reversibly tuned by varying the intensity of light. Under light illumination, the set voltage of the device decreases from 0.7 to 0.4 V. Due to the distinct output current of resistance states with and without light illumination, the device can function as a logic gate by switching voltage polarity and light intensity. This work provides new insights and suggests a measurement setup to further understand the resistive switching behavior in CsPbBr₃ thin films for future applications of optoelectronic memristors in logic circuits, digital data storage, the internet of things, and neuromorphic computing.

Introduction

Optoelectronic memristors are potential candidates for constructing multifunctional devices which can be responsive to both electrical and optical excitation [1]. Light-sensitive materials are highly desired to enhance the optical response of the optoelectronic memristors. To this aim, inorganic halide perovskites are extensively investigated owing to their excellent light absorption capability [2]. ABX_3 is the general chemical formula representing perovskite materials. A and B are cations, and X is the anion. Recently, these materials are widely used in various applications and devices, including photodetectors, light-emitting diodes, transistors, and solar cells [3]–[5]. The energy bandgap of inorganic halide perovskites is tunable, and they can be synthesized in the form of thin films and quantum dots [6]. Therefore, these materials are expected to become essential components for the next generation of optoelectronic devices in the near future.

In addition, these promising materials show memristive properties as well which is highly desired in optoelectronic memristors. Memristors (memory + resistor) were first introduced by Leon Chua in 1971 [7]. A memristor can be defined as a two-terminal device that exhibits a pinched hysteresis loop in the current-voltage characterization when stimulated by the electric field. Memristors are traditionally built from metal oxides [8] or organic materials [9] sandwiched between two electrodes. Among perovskite materials, $CsPbBr_3$ thin films demonstrate high photosensitivity and memristivity [10] which make them an ideal choice for fabricating optoelectronic memristors. Until now, most of the research works are focused on either the memristive property or optoelectronic application of perovskite materials. Therefore, it is desirable to develop device structures that enable the integration of both memristivity and photosensitivity properties in one device. Recently, optoelectronic memristors are designed and fabricated to perform binary arithmetic tasks [11]. Although the proposed devices are operating at low power

consumption, further investigations are required to improve the resistive switching stability, uniformity, and retention time.

In this work, we propose a device that can function as a photodetector and memristor simultaneously. We use $CsPbBr_3$ thin films to benefit from the high photosensitivity and memristive properties of these materials. A gold-coated probe tip is used as the top electrode to allow effective light illumination and minimize the shadowing effect on the materials. Moreover, the Au-coated tip helps to confine the growth and formation of conductive filaments in $CsPbBr_3$ thin films. The memconductance of the fabricated device is reversible by varying the light intensity.

Experimental

The fabrication process of the device is facile and straightforward. The thin film coatings of fluorine-doped tin oxide (FTO) on glass were used as the substrate. The substrate was rinsed ultrasonically using isopropanol, acetone, methanol, and deionized water. The one-step deposition method was used to prepare the $CsPbBr_3$ solution. Briefly, 0.4 molar of CsBr and PbBr2 in DMSO was mixed and stirred for 2 hours. The obtained clear solution was spin-coated onto the FTO at 2000 rpm. The resulting thin film of $CsPbBr_3$ is annealed at 100 ℃ for 10 minutes. The spin coating process can be repeated several times to achieve desired uniformity and thickness of thin films. For current-voltage (I-V) characterization, two probe tips are coated with 50 nm-thick gold (Au) using Angstrom Nexdep electron beam evaporator at room temperature. The vacuum pressure was kept at 6×10^{-7} Torr during the deposition process. We used a solar simulator as a light source with adjustable light intensities and spectrum from UV to near-infrared. The Keithley 4200 SCS parameter analyzer is utilized for the current–voltage (I-V) characterization of the fabricated devices. All the measurements were performed at room temperature.

Results and discussion

Figure 4.1(a) plots the XRD results of the prepared CsPbBr$_3$ thin films on glass. There are two distinct characteristic peaks at 15.6°, and 31.2°, ascribed to the (100), and (200) crystal planes of cubic CsPbBr$_3$ [12]. The optical absorption and photoluminescence (PL) spectra of CsPbBr$_3$ thin films are shown in Figure 4.1(b). The excitonic absorbance peak centers at 517 nm and the PL peak centers around 528 nm and the corresponding bandgap is estimated to be around 2.3 eV. Therefore, the fabricated device using CsPbBr$_3$ thin films is mostly sensitive to visible light and green lasers.
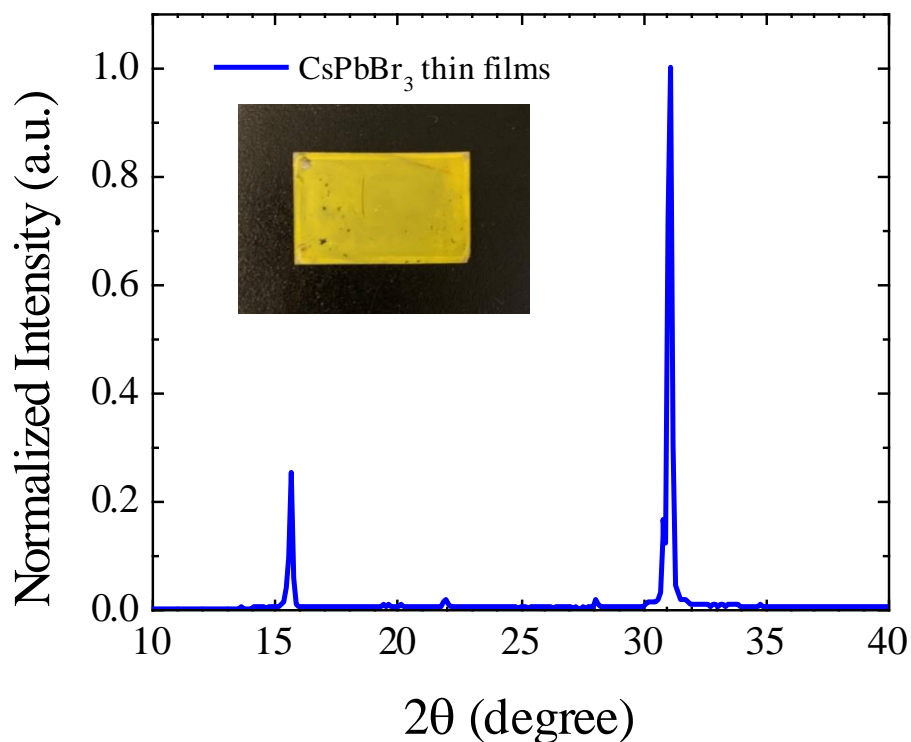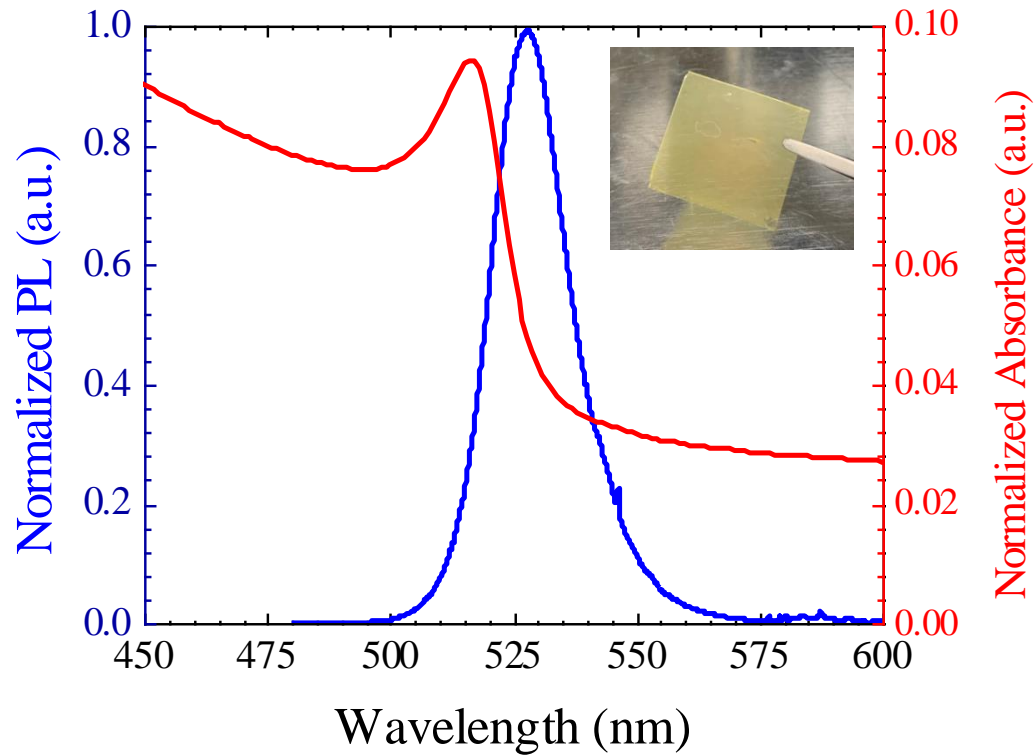
(a)

Figure 4.1. (a) XRD pattern of CsPbBr$_3$ thin films. (b) Photoluminescence (blue) and Absorbance (red) spectra of CsPbBr$_3$ thin films. A picture of the thin film on glass is shown in the inset.

Cont. (b)

To investigate the light sensitivity of the synthesized material (CsPbBr$_3$), an interdigital photodetector is fabricated and characterized. The fabrication process is demonstrated in Figure 4.2. A glass substrate is used to fabricate a device with Au/CsPbBr$_3$/Au structure, 50 nm-thick interdigital gold (Au) electrodes with the 10 µm finger-spacing are deposited using the photolithography method followed by the electron beam evaporation and lift-off process. The CsPbBr$_3$ solution is spin-coated onto the device at 2000 rpm for 30 seconds. In the last step, the device is annealed at 100 ℃ for 10 minutes and wire bonded for current-voltage characterizations.
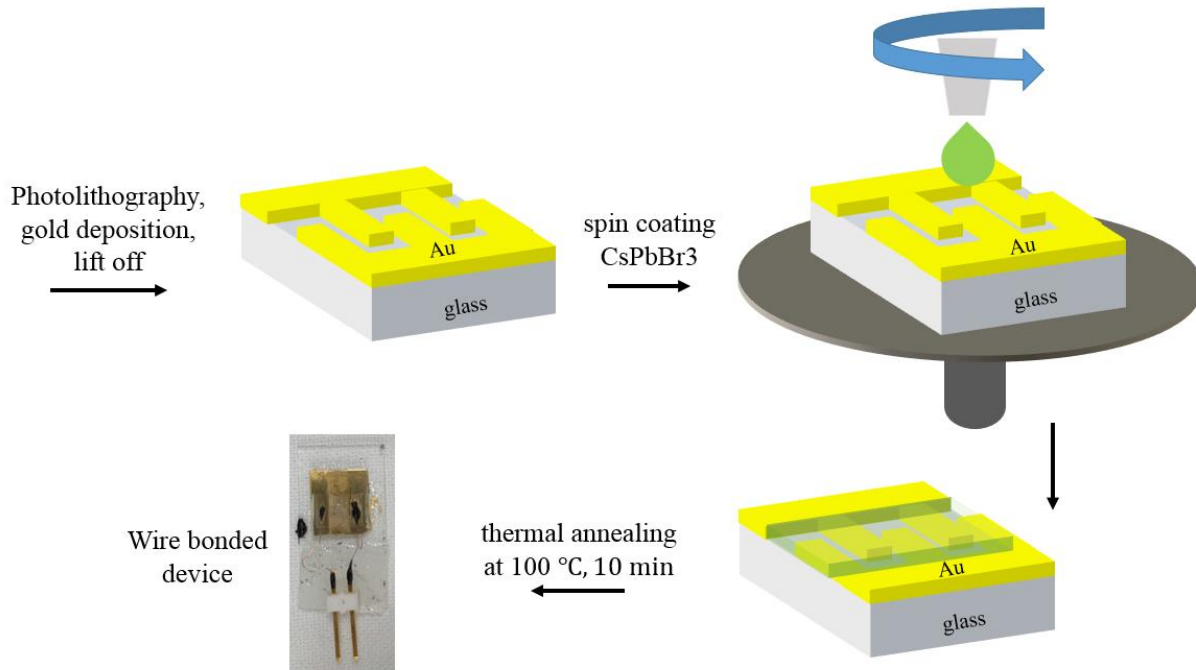
Figure 4.2. The fabrication process of CsPbBr$_3$ thin films photodetectors.

A solar simulator with a spectral range from UV to near-infrared is used to illuminate the device. The light intensity is tunable from 1 to 100 mW/cm^2 and the bias voltage starts from -5 V to +5 V shown in Figure 4.3(a). Figure 4.3(b) shows the I-V characterization of the device. The photocurrent to dark current ratio is almost two orders of magnitude. The device can function as a self-powered photodetector since it is optically active at 0 V bias voltage. The time response of the device is shown in Figure 4.3(c). The output current is measured at 4 V bias voltage while the light is switched on and off every 10 seconds. The spectral response of the device is measured using Bruker 125 HR Fourier transform infrared (FTIR) spectrometer. The spectral response is defined as photocurrent over incident optical power at specific wavelengths. Figure 4.3(d) demonstrates the spectral response of the device from 350 to 700 nm. The corresponding response is confined between 380 and 550 nm. The cut-off wavelength depends on the CsPbBr$_3$ bandgap, which is around 2.3 eV, thus, photons with lower energy cannot be absorbed. At shorter

wavelengths, the response decays due to the restriction of the beam splitter inside the spectrometer. The beam splitter absorbs light in the UV region and completely obscures the signal at 380 nm and shorter wavelengths. The obtained results indicate excellent optical properties of CsPbBr$_3$ thin films, suggesting potential applications in optoelectronic devices. Therefore, we use CsPbBr$_3$ thin films as a light-sensitive switching layer in the proposed device. The fabrication process of the new device is explained in the experimental section.
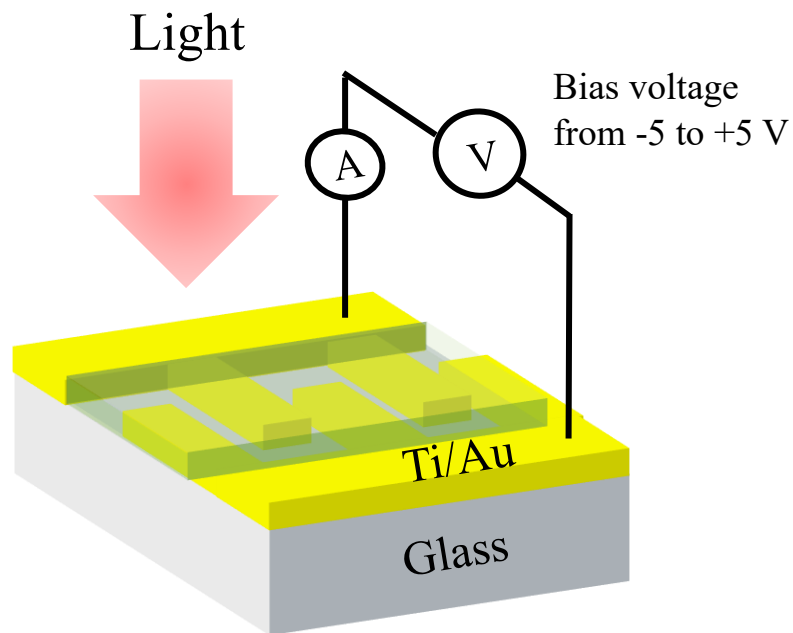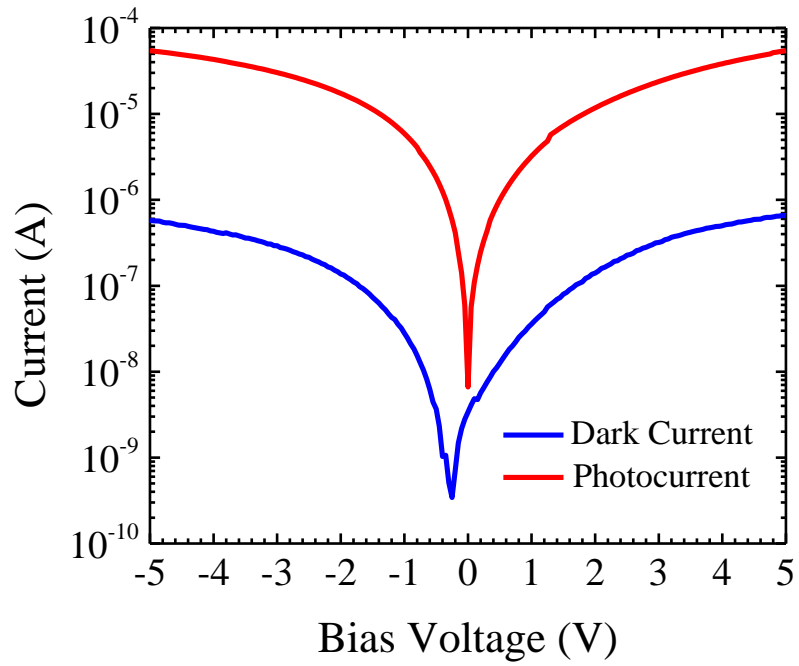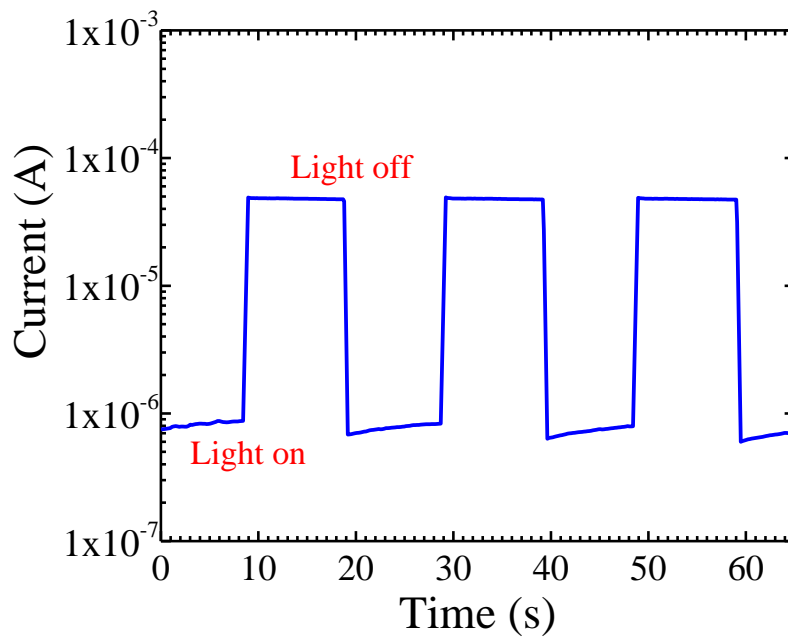
(a)

Figure 4.3. (a) A schematic picture of the fabricated device. (b) The current-voltage characteristics of the CsPbBr3 photodetector measured under dark and light illumination. (c) The time response of the CsPbBr3 photodetector at 4 V. (d) The spectral response of the CsPbBr3 photodetector.
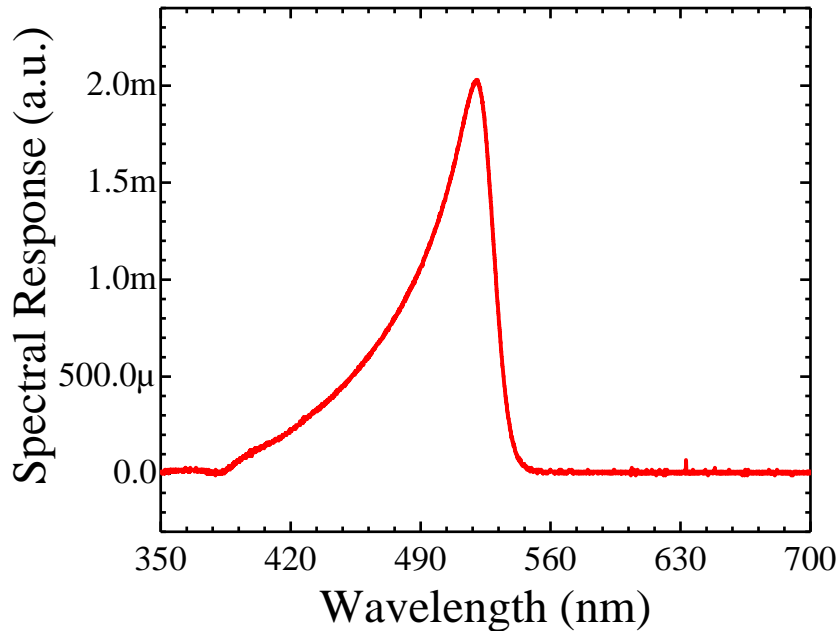
Cont. (b)

Cont. (c)

Cont. (d)

After the synthesis of thin films, spin coating process, and annealing, the device CsPbBr$_3$/FTO is ready for current-voltage (I-V) characterization. One of the Au-coated tips is used as the top electrode and the other one is connected to the FTO as is shown in Figure 4.4(a). The idea is to minimize the surface electrode area on the top to reduce the generation of conductive filaments with different lengths [13]. The concept is shown in Figure 4.4(b). A solar simulator is used as a light source with adjustable light intensities from 1 to 30 mW/cm^2. The device is characterized at room temperature under different light intensities. The input voltage sweeps back and forth between -3 V to +3 V while the output current is recorded. The resistive switching behavior is apparent from Figure 4.5 that shows the I-V characteristics of the device based on CsPbBr$_3$ thin films. There are sudden transitions between the high resistance state and the low resistance state. Figure 4.5(a) demonstrates the I-V characteristics of the device in the dark condition, the input voltage sweeps from -3 V to +3 V and the device sets to the low resistance state at + 0.7 V. While the negative voltage bias is applied from +3 V to -3 V, the device resets to

the high resistance state at -0.8 V. Figure 4.5(b) depicts the I-V characteristics of the device under the light illumination, the device sets to the LRS at 0.4 V and the reset voltage is around -0.9 V.
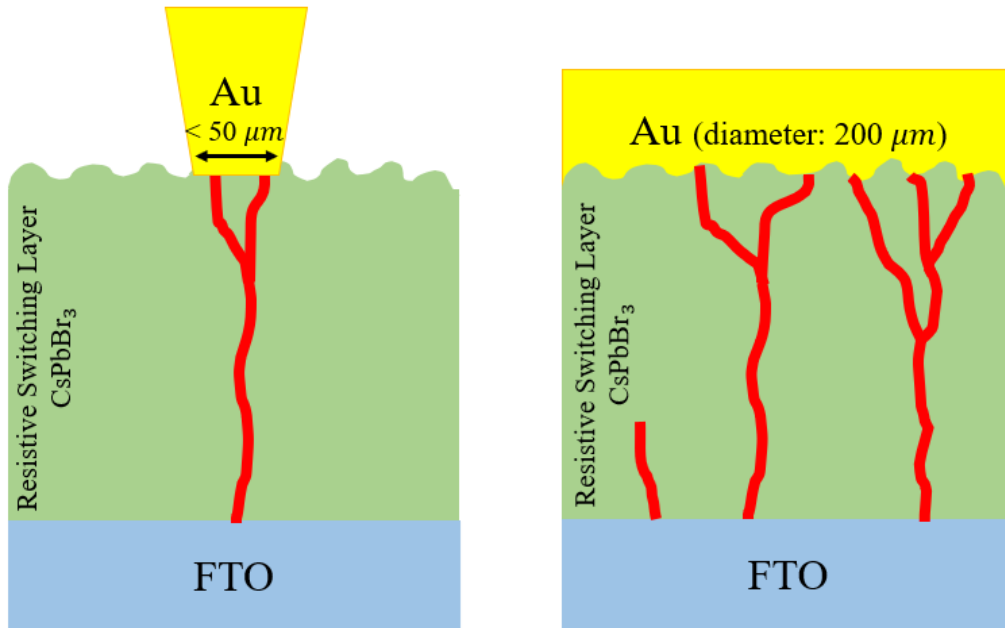
(a)
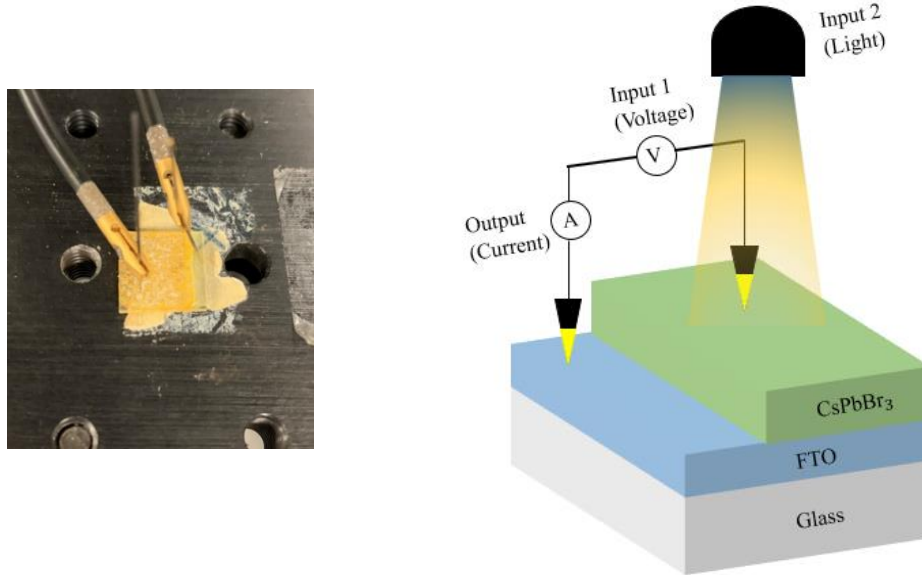
(b)

Figure 4.4. (a) A schematic picture (left) and the structure of the fabricated device (right). (b) The large surface electrode area on the top (right) may produce multiple conductive filaments with different lengths. The electrode tip with a small surface area may minimize the generation of conductive filaments.

The resistive switching behavior is consistent over multiple switching cycles. Figure 4.5(c) shows the stability and switching cycles endurance in the device under light illumination. The transitions between HRS and LRS are uniform and repeatable. Figure 4.5(d) compares the I-V characteristics of the device with and without light illumination. The SET voltage is reduced from 0.7 to 0.4 V as we increase the light intensity.
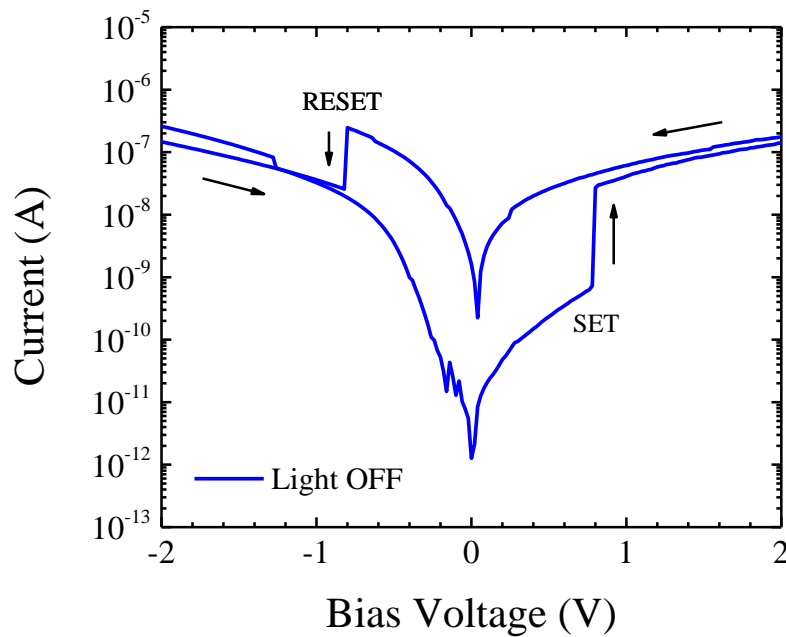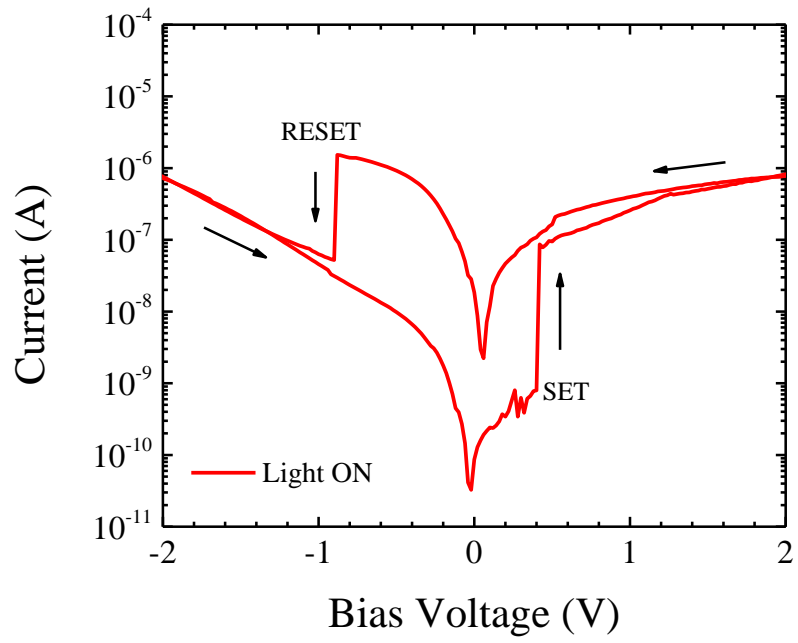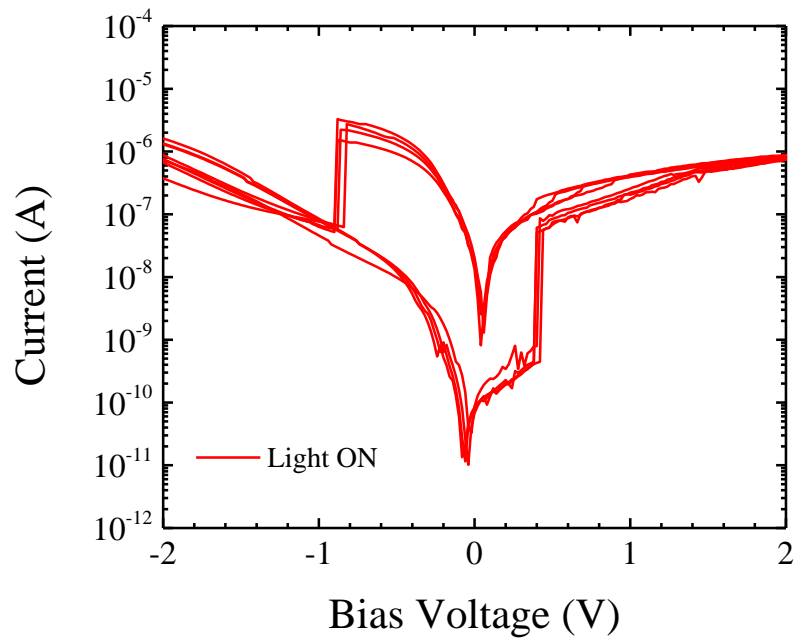
(a)

Figure 4.5. (a) The I-V characteristics of the device in the dark condition. (b) The I-V characteristics of the device under the light illumination. (c) Resistive switching endurance of the device under light illumination. (d) The I-V characteristics of the device with (red) and without (blue) light illumination.
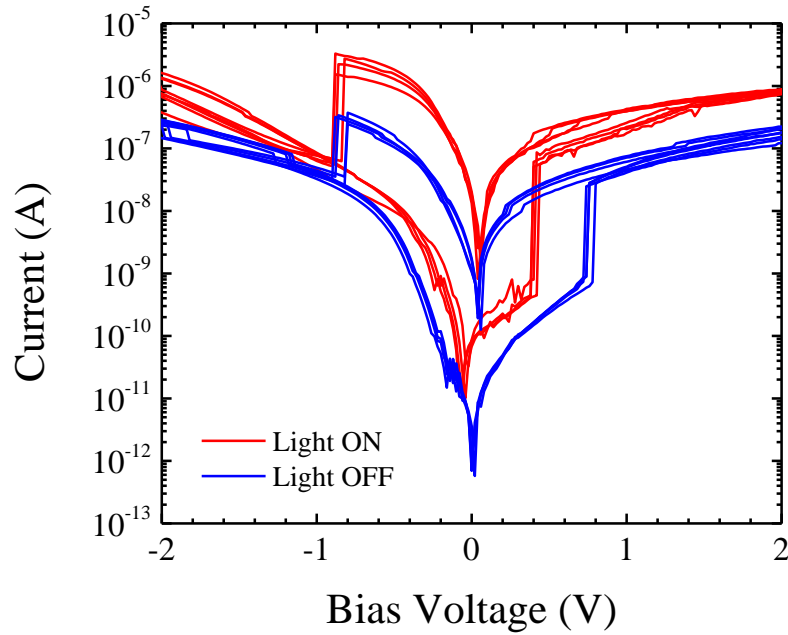
Cont. (b)

Cont. (c)

Cont. (d)

Figure 4.6 demonstrates the set voltages of the device under different light intensities. The set voltage is light-dependent and exponentially decreases from 0.78 to 0.43 V as the light intensity increases from 1 to 50 mW/cm^2. To better understand the resistive switching behavior, the effect of light illumination on the migration of Bromide (Br$^-$) ions in CsPbBr$_3$ must be considered. After applying bias voltage on the device, the Br$^-$ ions migrate toward the anode (Au) and Br$^-$ ↔ Br + e$^-$. Meanwhile, the bromide vacancies (V_{Br}^+) form conductive filaments inside the thin film, and the device sets from HRS to LRS. On the other hand, the Br$^-$ ions diffuse into the thin film once the bias voltage is reversed and the device resets back from LRS to HRS. To further explain the photoassisted switching mechanism in the device, the formation of bromide vacancies is considered. Under light illumination, photoexcited carriers including electrons and holes are generated in the CsPbBr$_3$ layer. By applying the electric field, electron-holes pairs are separated and drift toward electrodes, increasing the photocurrent. The Schottky barrier between the CsPbBr$_3$ layer and Au is decreased due to the increase of hole concentration at the interface. Thus, the

60

contact between the CsPbBr$_3$ layer and the Au electrode becomes a quasi-ohmic contact [14]. The photoexcited holes combine with bromide ions h$^+$ + Br$^-$ $\leftrightarrow$ Br, resulting in the accumulation of bromide vacancies, which facilitates the formation of conductive filaments [15]. Figures 4.7 (a) and (b) demonstrate the resistive switching mechanism of the device in dark, and under light illumination, respectively.
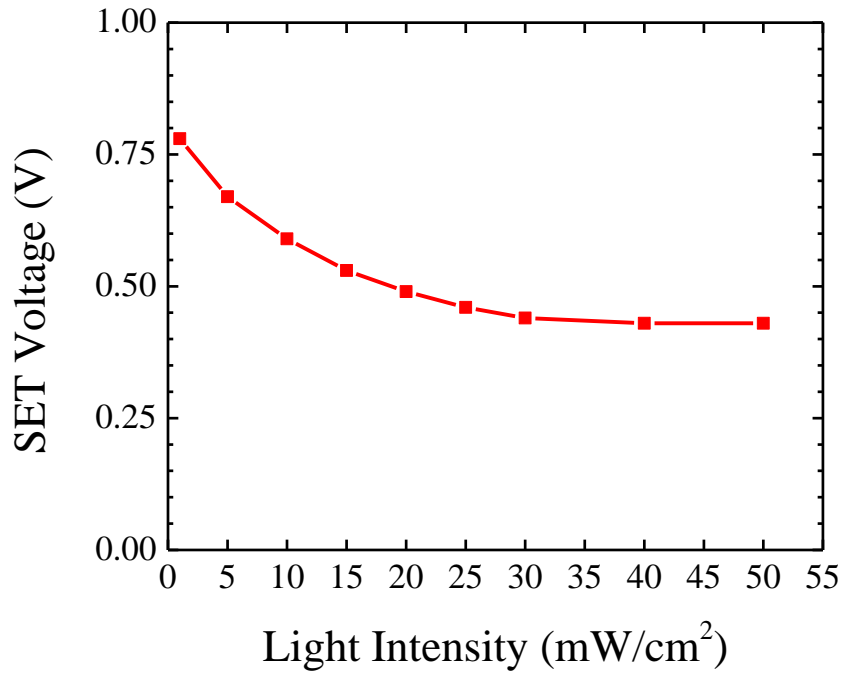
Figure 4.6. The SET voltage of the device under different light intensities.

(a)

$$Br^- \leftrightarrow Br + e^-$$

(b)

$$Br^- \leftrightarrow Br + e^-$$
$$Br^- + h^+ \leftrightarrow Br$$
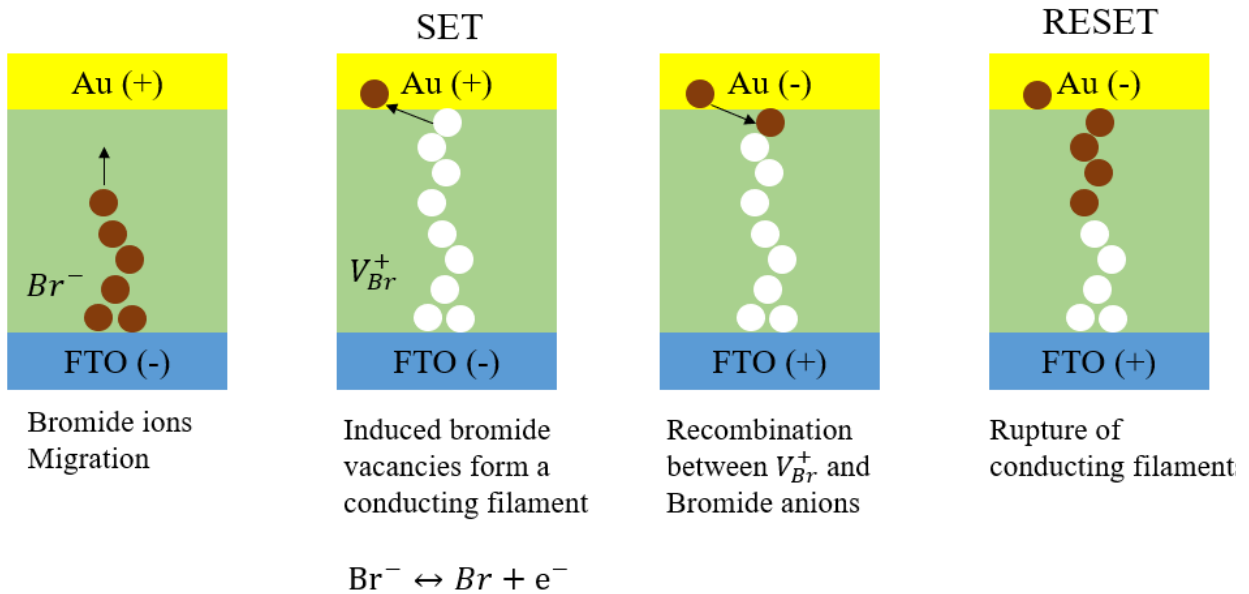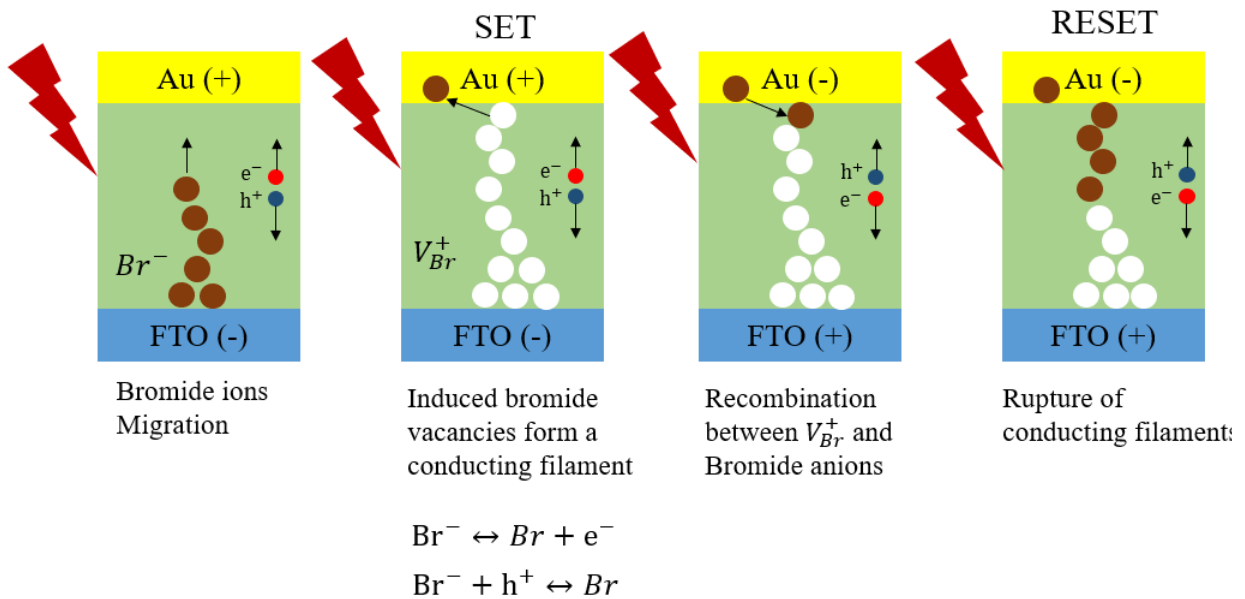
Figure 4.7. The resistive switching behavior of the device and the formation of conductive filaments (a) in dark (b) under light illumination.

The bias voltage and light illumination affect the Schottky barrier between the metal and resistive switching layer in memory resistors [14]. Figure 4.8(a) demonstrates a schematic of the

band diagram of the junction between Au and CsPbBr$_3$ in dark. Due to the difference between the work functions of Au and CsPbBr$_3$ ($\boldsymbol{\phi}_{Au} > \boldsymbol{\phi}_{CsPbBr3}$) a Schottky barrier forms at the interface of the Au and CsPbBr$_3$ thin film. Therefore, the electrons move from the CsPbBr$_3$ thin film to the Au because of the higher Fermi level in the CsPbBr$_3$ layer and trapped holes remain in the CsPbBr$_3$ thin film. As a result, a depletion region, and a built-in electric field form at the Au/CsPbBr$_3$ interface. The internal electric field hinders further carriers transport, and the device stabilizes at the high resistance state. As the positive voltage bias is applied and exceeds the SET voltage, the depletion region and internal electric field are weakened and the injected holes accumulate at the interface, lowering the E$_F$ and Schottky barrier. Thus, the contact becomes quasi-ohmic and the device switches to the low resistance state. When the negative voltage is applied, the injected holes move back from the CsPbBr$_3$ layer to the Au electrode, and the Schottky barrier increases. As a result, the device resets back to its original high resistance state. Figure 4.8(b) depicts a schematic of the band diagram of the junction between Au and CsPbBr$_3$ under light illumination. The photogenerated electrons are excited in the CsPbBr$_3$ layer and move from the valence band to the conduction band, leaving holes behind in the valence band. Therefore, the holes concentration increases at the interface which shifts the Fermi level to the valence band and decreases the Schottky barrier and depletion region, facilitating the electrons transport at the Au/CsPbBr$_3$ interface. At the same time, extra holes are injected from the Au into the interface, reducing the barrier more significantly compared to the dark condition. Thus, the light illumination can affect the SET voltage of the device as shown in Figure 4.6. As the light intensity increases, a larger number of carriers are generated that intensify the effects mentioned above and a smaller external voltage is required to inject holes [16]. The constant light illumination neutralizes the carriers recombination rate and the photocurrent increases as shown in Figure 4.5(d). Therefore, the device

functions as a photodetector as well. When the negative voltage is applied under the light illumination, the photocurrent still increases compared to the dark condition due to excess photogenerated carriers. The electrons move toward the FTO and holes drift back to the Au, bringing the Schottky barrier to its initial state.

(a)

(b)

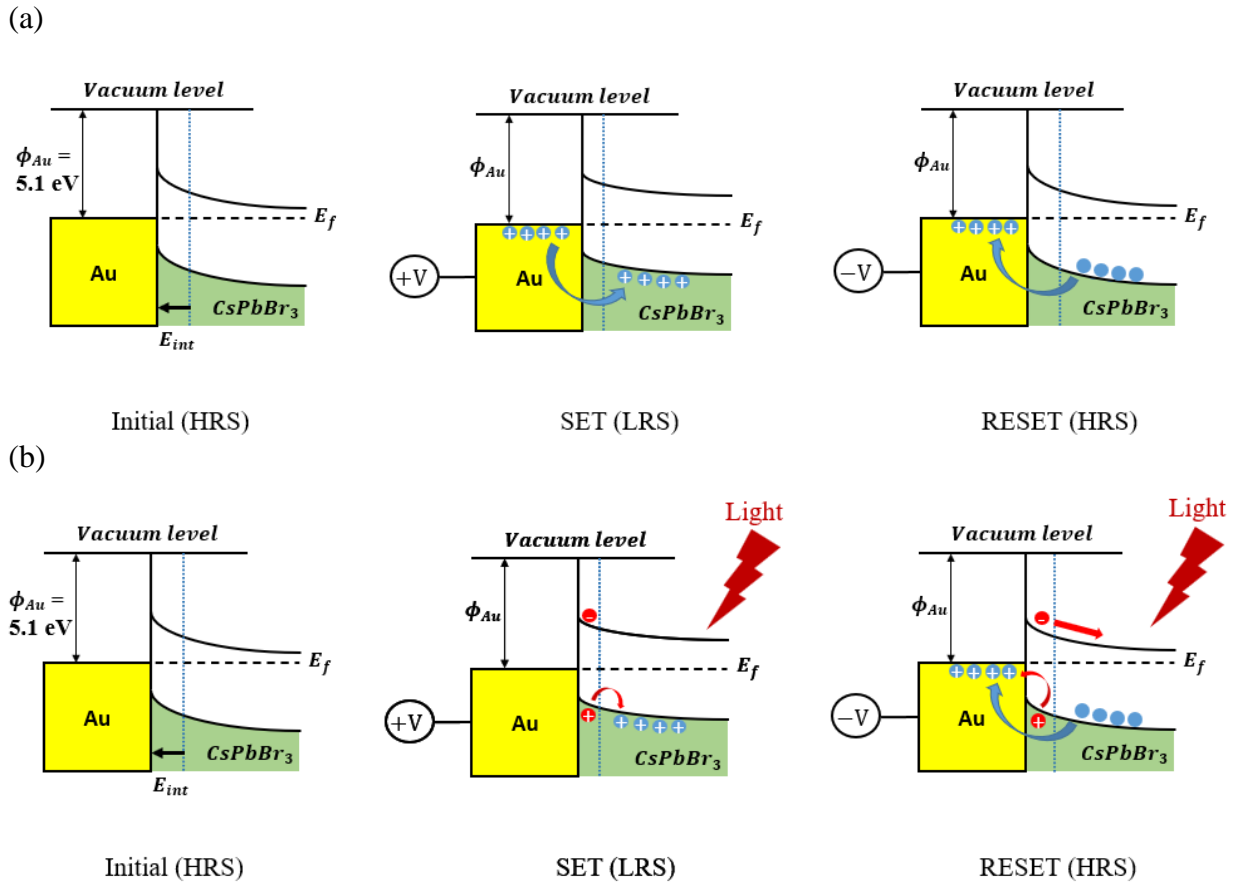Figure 4.8. The resistive switching mechanism in the Au/CsPbBr$_3$/FTO device. (a) in dark. (b) Under the light illumination.

Conclusion

In summary, we designed and fabricated a photomemristor in which the photocurrent and resistive switching behavior of the device can be adjusted under light illumination. A device structure of Au/ CsPbBr$_3$/FTO is fabricated and characterized. The CsPbBr$_3$ thin films are

separately used in a photodetector which shows high photosensitivity and responsivity. The I-V characteristics indicate high stability and good endurance as well as low operation voltage of the memristor. The effect of light illumination on the resistive switching behavior was explained using the migration of bromide vacancies, Schottky barrier, and the band diagram at the Au/ $CsPbBr_3$ interface. The set voltage of the fabricated memristor decreases as the light intensity increases. This device can execute multiple tasks by combining electrical and optical inputs. Therefore, the fabricated photomemristor offers promising applications in logic circuits, digital data storage, the internet of things, and neuromorphic computing.

References

[1] X. Zhao, H. Xu, Z. Wang, Y. Lin, and Y. Liu, "Memristors with organic-inorganic halide perovskites," *InfoMat*, p. inf2.12012, May 2019, doi: 10.1002/inf2.12012.

[2] W. Xiang and W. Tress, "Review on Recent Progress of All-Inorganic Metal Halide Perovskites and Solar Cells," *Adv. Mater.*, vol. 31, no. 44, p. 1902851, Nov. 2019, doi: 10.1002/adma.201902851.

[3] A. K. Jena, A. Kulkarni, and T. Miyasaka, "Halide Perovskite Photovoltaics: Background, Status, and Future Prospects," *Chem. Rev.*, vol. 119, no. 5, pp. 3036–3103, Mar. 2019, doi: 10.1021/acs.chemrev.8b00539.

[4] G. Pacchioni, "Highly efficient perovskite LEDs," *Nat. Rev. Mater.*, vol. 6, no. 2, pp. 108–108, Feb. 2021, doi: 10.1038/s41578-021-00280-5.

[5] Y. Liu, P.-A. Chen, and Y. Hu, "Recent developments in fabrication and performance of metal halide perovskite field-effect transistors," *J. Mater. Chem. C*, vol. 8, no. 47, pp. 16691–16715, 2020, doi: 10.1039/D0TC03693E.

[6] S. Wei, Y. Yang, X. Kang, L. Wang, L. Huang, and D. Pan, "Room-temperature and gram-scale synthesis of $CsPbX_3$ (X = Cl, Br, I) perovskite nanocrystals with 50–85% photoluminescence quantum yields," *Chem. Commun.*, vol. 52, no. 45, pp. 7265–7268, 2016, doi: 10.1039/C6CC01500J.

[7] L. Chua, "Memristor-The missing circuit element," *IEEE Trans. Circuit Theory*, vol. 18, no. 5, pp. 507–519, 1971, doi: 10.1109/TCT.1971.1083337.

[8] D. B. Strukov, G. S. Snider, D. R. Stewart, and R. S. Williams, "The missing memristor found," *Nature*, vol. 453, no. 7191, pp. 80–83, May 2008, doi: 10.1038/nature06932.

[9] L. Yuan, S. Liu, W. Chen, F. Fan, and G. Liu, "Organic Memory and Memristors: From Mechanisms, Materials to Devices," *Adv. Electron. Mater.*, vol. 7, no. 11, p. 2100432, Nov. 2021, doi: 10.1002/aelm.202100432.

[10] Y. Li *et al.*, "High-performance perovskite photodetectors based on solution-processed all-inorganic $CsPbBr_3$ thin films," *J. Mater. Chem. C*, vol. 5, no. 33, pp. 8355–8360, 2017, doi: 10.1039/C7TC02137B.

[11] G. Lin *et al.*, "An organic–inorganic hybrid perovskite logic gate for better computing," *J. Mater. Chem. C*, vol. 3, no. 41, pp. 10793–10798, 2015, doi: 10.1039/C5TC02270C.

[12] W. Yan *et al.*, "Determination of complex optical constants and photovoltaic device design of all-inorganic $CsPbBr_3$ perovskite thin films," *Opt. Express*, vol. 28, no. 10, p. 15706, May 2020, doi: 10.1364/OE.392246.

[13] V. R. Nallagatla, J. Jo, S. K. Acharya, M. Kim, and C. U. Jung, "Confining vertical conducting filament for reliable resistive switching by using a Au-probe tip as the top

electrode for epitaxial brownmillerite oxide memristive device," *Sci. Rep.*, vol. 9, no. 1, p. 1188, Dec. 2019, doi: 10.1038/s41598-018-37986-6.

[14] F. Zhou, Y. Liu, X. Shen, M. Wang, F. Yuan, and Y. Chai, "Low-Voltage, Optoelectronic $CH_3NH_3PbI_{3-x}Cl_x$ Memory with Integrated Sensing and Logic Operations," *Adv. Funct. Mater.*, vol. 28, no. 15, p. 1800080, Apr. 2018, doi: 10.1002/adfm.201800080.

[15] Y. Wang *et al.*, "Synergies of Electrochemical Metallization and Valance Change in All-Inorganic Perovskite Quantum Dots for Resistive Switching," *Adv. Mater.*, vol. 30, no. 28, p. 1800327, Jul. 2018, doi: 10.1002/adma.201800327.

[16] F. Lv *et al.*, "Resistive Switching Characteristics Improved by Visible-Light Irradiation in a Cs2AgBiBr6-Based Memory Device," *Nanomaterials*, vol. 11, no. 6, p. 1361, May 2021, doi: 10.3390/nano11061361.

Chapter 5: Conclusion

Over the course of this work, we have completed three experimental steps of the proposed project. In the first step, various types of quantum dots and thin films are used in different structures to fabricate memristors. For example, we reported a facile fabrication method and analyzed the resistive switching behavior of the heterogenous electrodes structure of FTO/CuO-Cu_2O/Au memristor. The copper oxide complex thin film is used as the switching layer, which is investigated by XRD, Raman, and UV-Vis spectroscopy. The conduction mechanism of the device follows the space charge limited conduction (SCLC) theory. The achieved I-V characterization results suggest high endurance, low SET voltage, and efficient power consumption of the device. However, further investigations are required to increase the retention time and on/off ratio in the proposed memristor.

In the second part of the work, multiple photodetectors are designed and fabricated using the same materials used to fabricate memristors in the first step of the work. For instance, we developed a UV-Visible copper oxide-based thin films photodetector, which demonstrates enhanced optoelectronic performances when the device is fabricated at higher annealing temperatures. The surface morphology of copper oxide thin films is engineered by thermal annealing to cover UV-Visible spectral range. We explained the I-V characterization results by the grain-structure model and the effects of the large grain size on the dark current, photocurrent, photosensitivity, responsivity and detectivity are investigated. We confirmed that the fabricated device is reliable by testing the detectivity performance for over eight weeks. Therefore, the obtained results reveal that the fabricated copper oxide photodetector is reliable and can be considered in practical optoelectronic applications.

In the last part of the work, we designed and fabricated a photomemristor in which the photocurrent and resistive switching behavior of the device can be adjusted under light illumination. A device structure of Au/ $CsPbBr_3$/FTO is fabricated and characterized. The $CsPbBr_3$ thin films are separately used in a photodetector which shows high photosensitivity and responsivity. The I-V characteristics indicate high stability and good endurance as well as low operation voltage of the memristor. The effect of light illumination on the resistive switching behavior was explained using the migration of bromide vacancies, Schottky barrier, and the band diagram at the Au/ $CsPbBr_3$ interface. The set voltage of the fabricated memristor decreases as the light intensity increases. This device can execute multiple tasks by combining electrical and optical inputs. Therefore, the fabricated photomemristor offers promising applications in logic circuits, digital data storage, the internet of things, and neuromorphic computing.

Overall, this work provides new insights and suggests a measurement setup to further understand the resistive switching behavior in metal oxide and perovskite thin films for future applications of optoelectronic memristors in logic circuits, digital data storage, the internet of things, and neuromorphic computing.

Appendix A: ZnO quantum dots characterization

Synthesis: first, 0.48 g potassium hydroxide was stirred and dissolved in 25 ml methanol. Then, the obtained solution was added dropwise into 0.1 M solution of zinc acetate dihydrate in methanol. The mixture was stirred at 60 °C for 2 hours. The obtained white precipitate was washed with methanol and centrifuged 3 times. The zinc oxide quantum dots precipitate as shown in Figure A.1and was dried under the vacuum overnight. The dried precipitate was smashed several times to collect fine white powder. The collected powder was dispersed in 1-buthanol and ethanol for further characterizations. Figure A.2 demonstrates the absorbance spectra of the zinc oxide quantum dots solution. The excitonic peak centered at 351 nm ~ 3.5 eV. The inset illustrates the Tauc plot and the calculated bandgap of 3.18 eV. Figure A.3 shows the Raman spectra and phonon modes of ZnO quantum dots thin films.
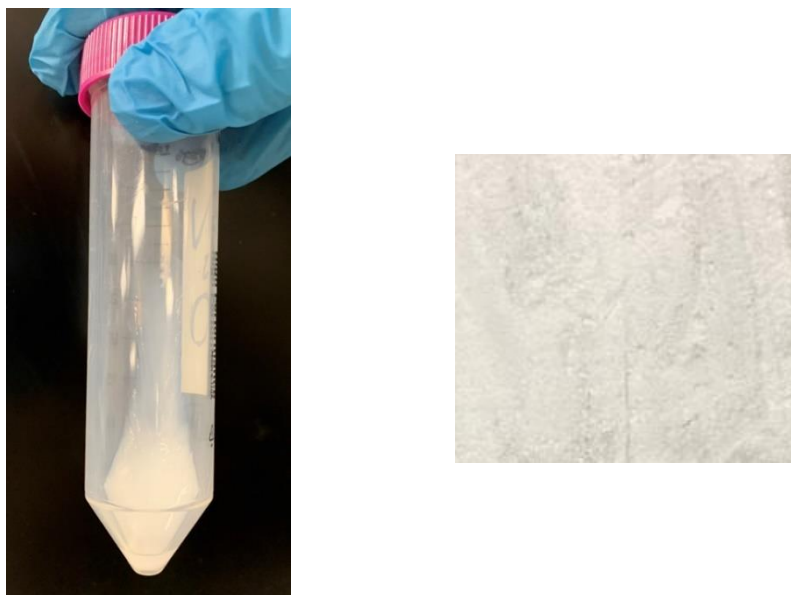

Figure A.1. Pictures of precipitated ZnO quantum dots (left) and dried ZnO QDs powder (right) "Photo by Amir Shariffar"
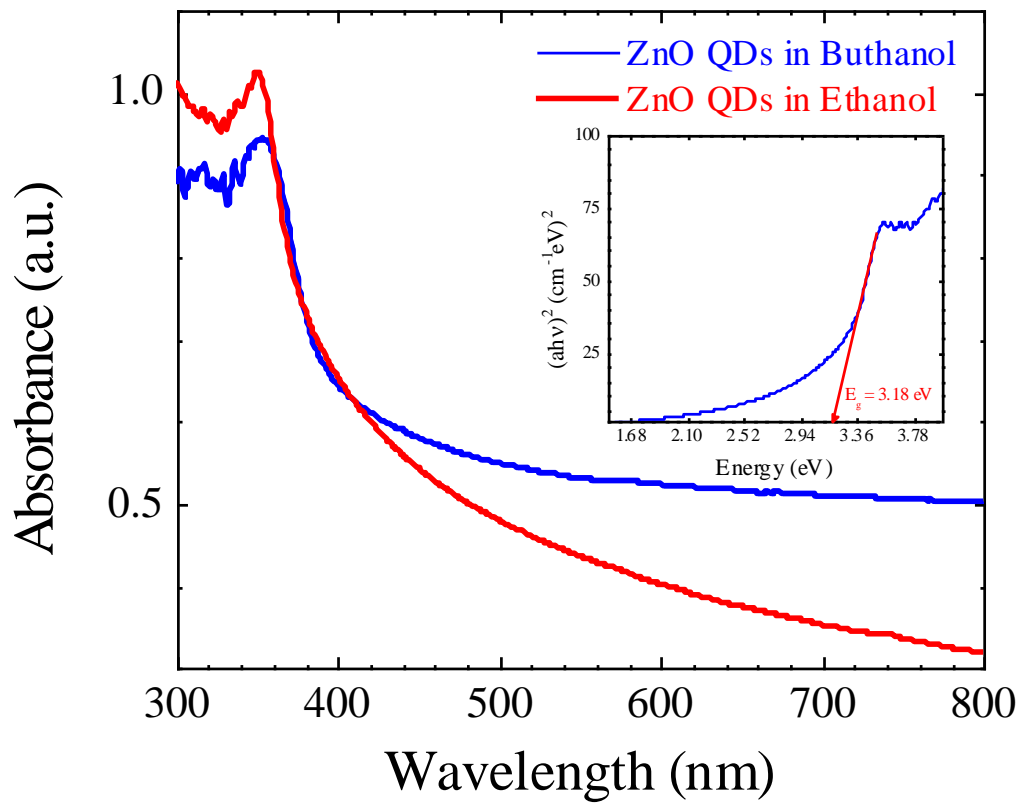
Figure A.2. The absorbance spectra of ZnO quantum dots. The inset illustrates the Tauc plot and the calculated bandgap of 3.18 eV.
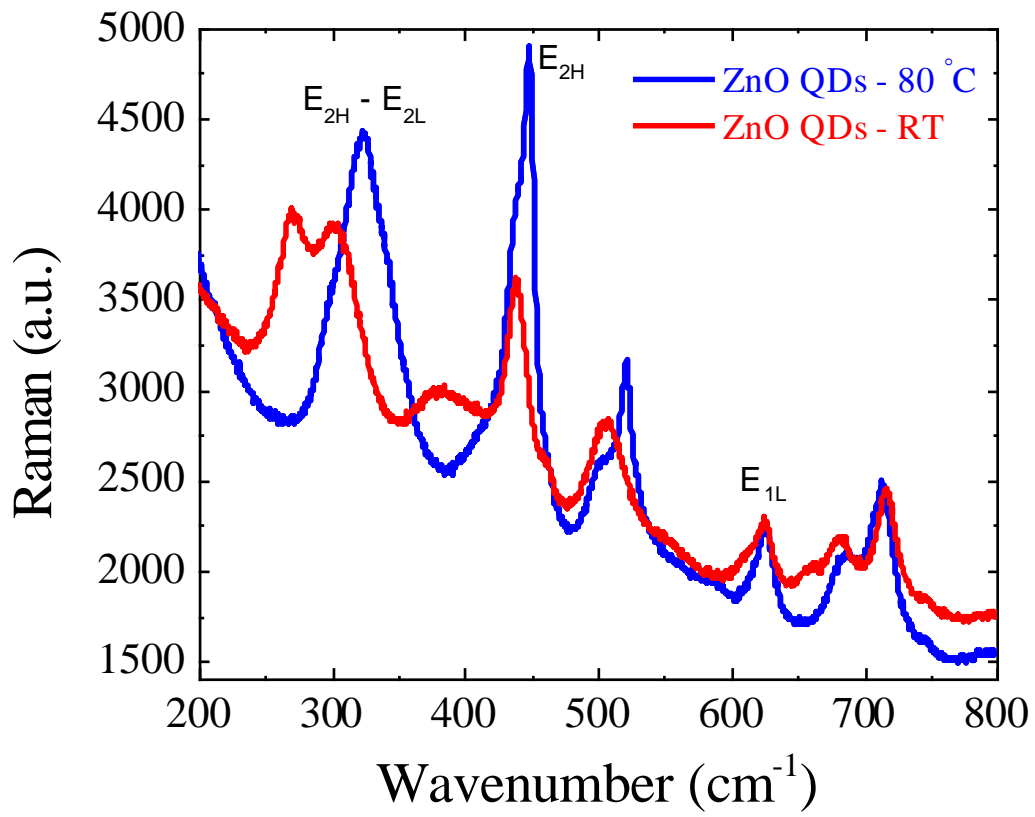
Figure A.3. the Raman spectra of ZnO quantum dots thin films on glass.

Appendix B: CsPbBr₃ quantum dots characterization

Synthesis: First, 147 mg of lead bromide (PbBr$_2$) and 85 mg cesium bromide (CsBr) were stirred and dissolved in 10 ml of dimethyl formamide (DMF) at the room temperature. Then, 1 ml of oleic acid and 0.5 ml of oleylamine were added to the solution. The reaction was allowed to continue for 30 minutes. The obtained solution was added dropwise into Chlorobenzene under vigorous stirring until a green emission was observed from the solution (Figure B.1). The absorbance, photoluminescence, and XRD results of CsPbBr$_3$ quantum dots are compared with CsPbBr3 thin films to show the quantum confinement effect in Figure B.2, B.3, and B.4.
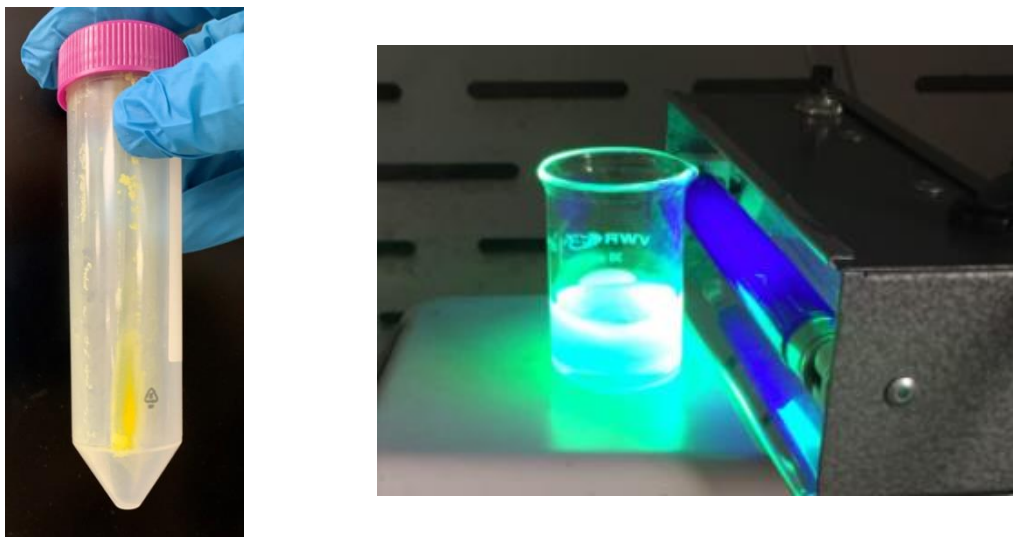

Figure B.1. Pictures of CsPbBr$_3$ quantum dots solution (right) and precipitated QDs (left). "Photo by Amir Shariffar"
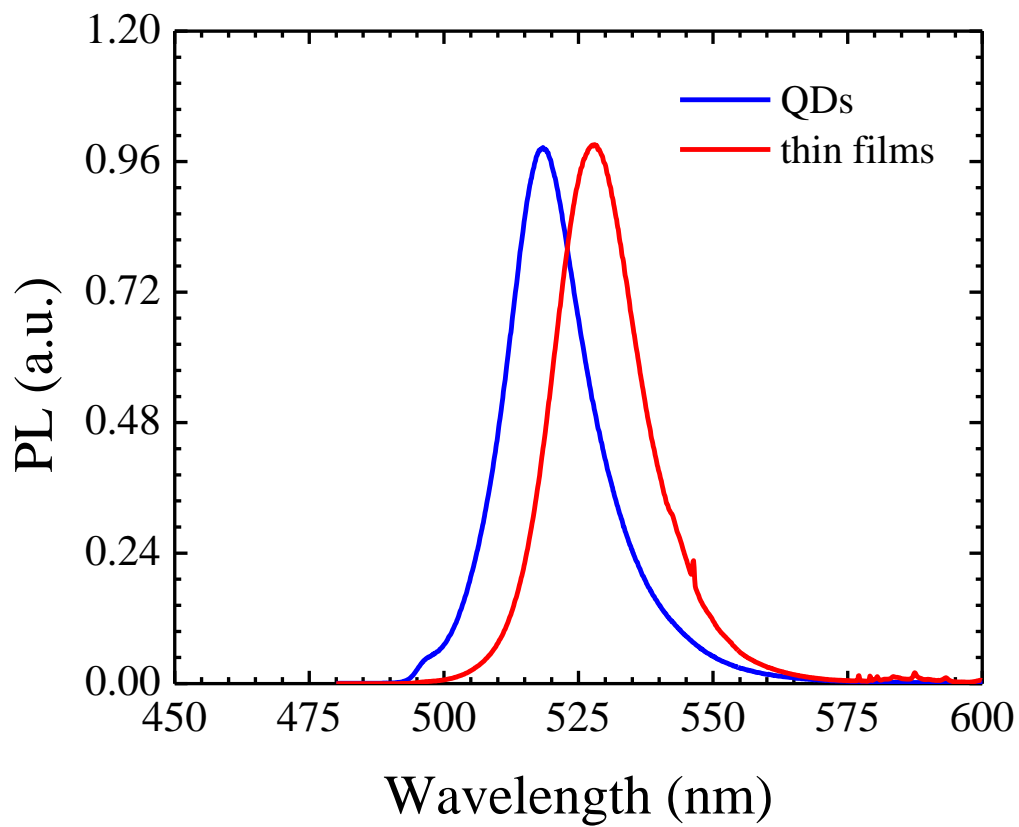
Figure B.2. The photoluminescence spectra of CsPbBr$_3$ Quantum Dots and thin films.
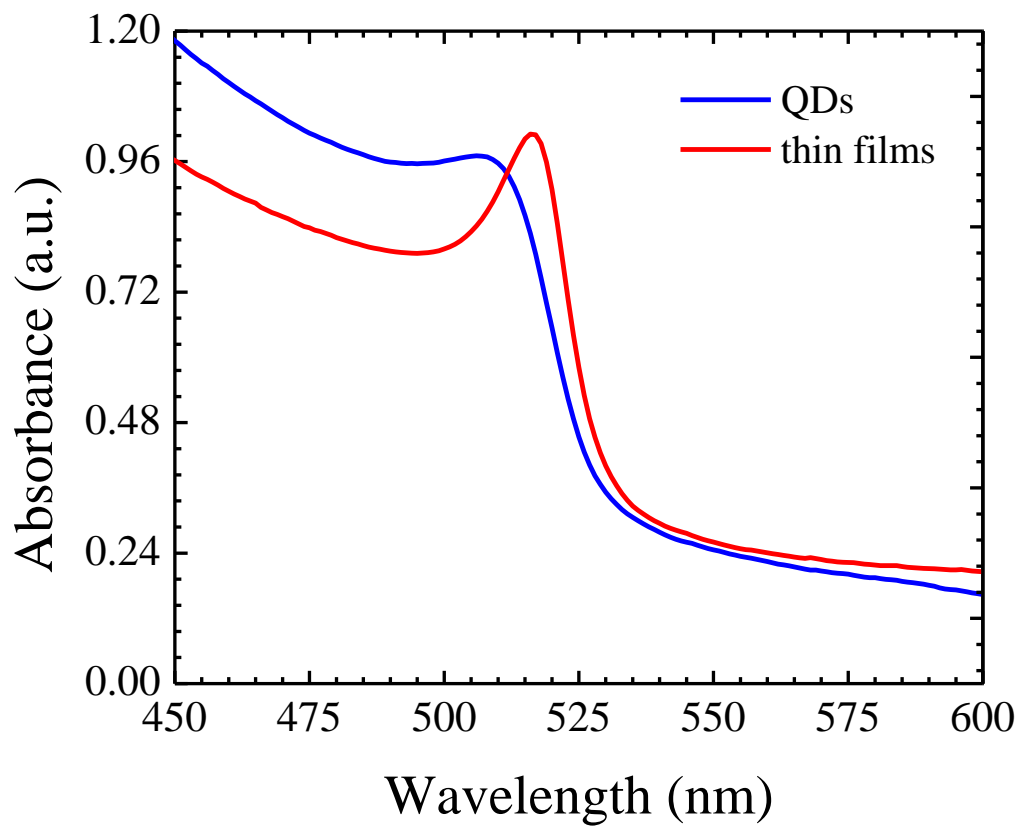
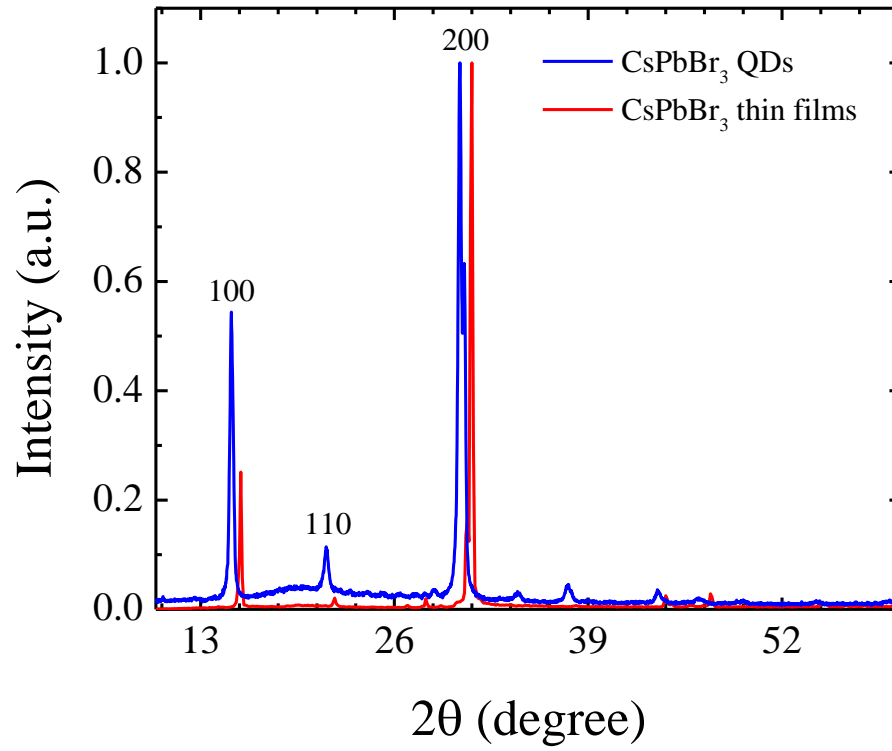Figure B.3. The absorbance spectra of CsPbBr$_3$ Quantum Dots and thin films.

Figure B.4. The XRD patterns of CsPbBr$_3$ Quantum Dots and thin films.

Appendix C: CuO self-powered photodetector

A self-powered photodetector is fabricated using copper oxide thin films annealed at 900 °C. The fabrication process contains two steps of photolithography, metallization, and lift off to achieve Au/CuO/Ti photodetector. Figure C.1 demonstrates the current-voltage characteristics of the device. There is two order of magnitude current ON/OFF ratio at 0 V, indicating the ability of the photodetector to generate open circuit voltage and short circuit current similar to solar cells. The Time-resolved current response at 5 and 0 V is shown in Figure C.2 and Figure C.3, respectively.
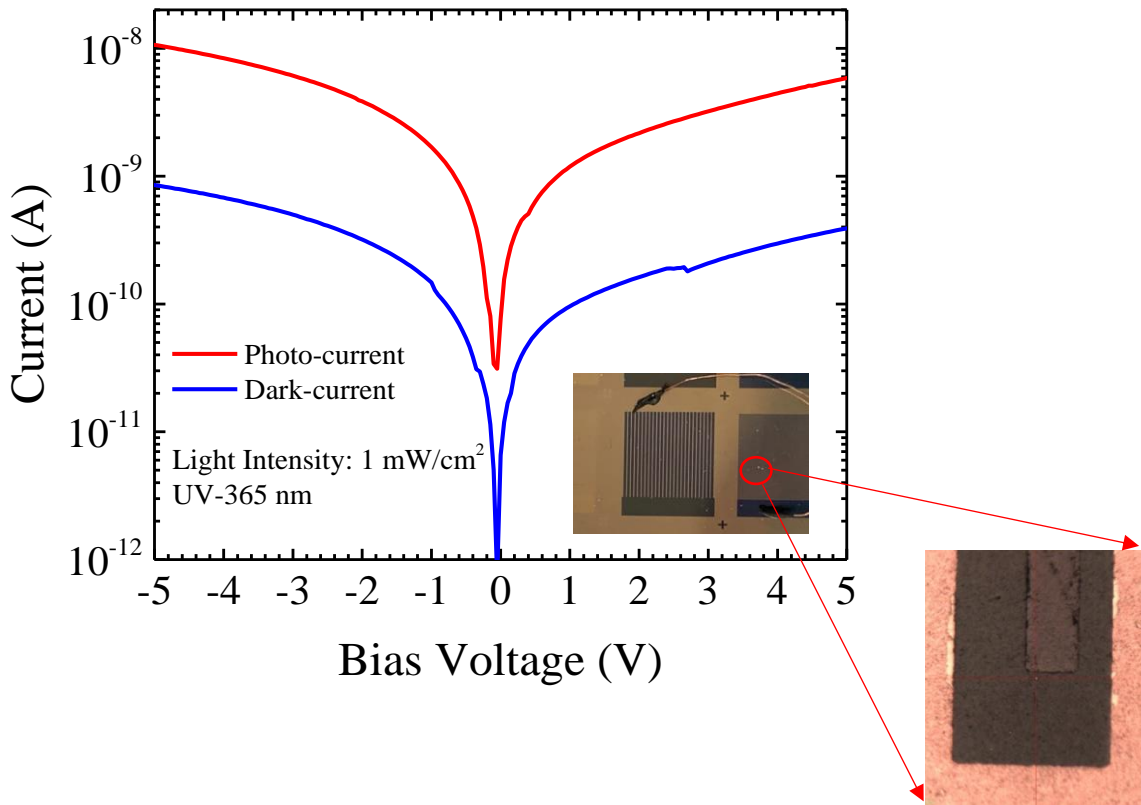

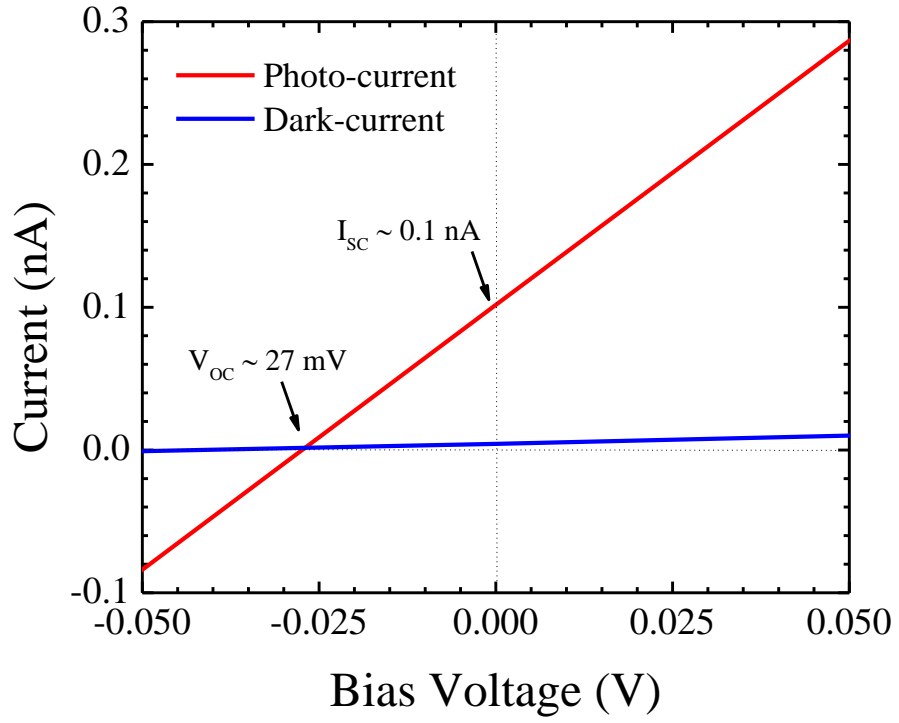Figure C.1. The current-voltage characteristics of the Au/CuO/Ti structure.

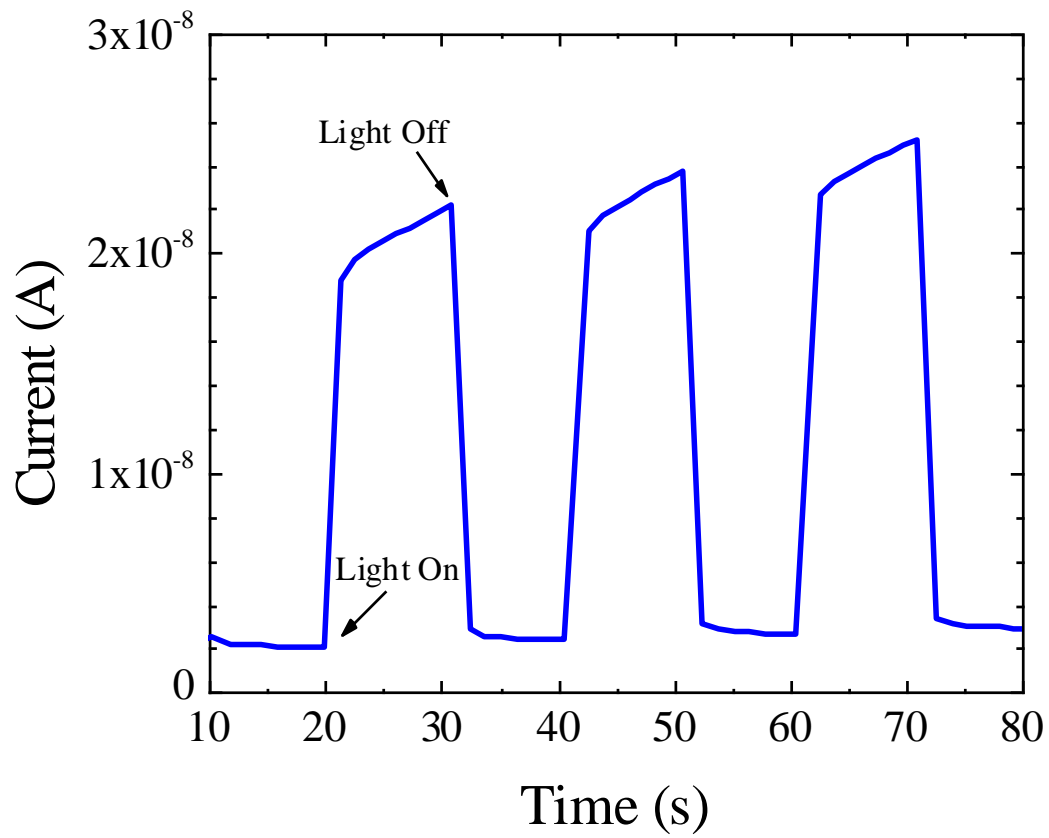Figure C.2. The open circuit voltage and short circuit current of the self-powered photodetector.

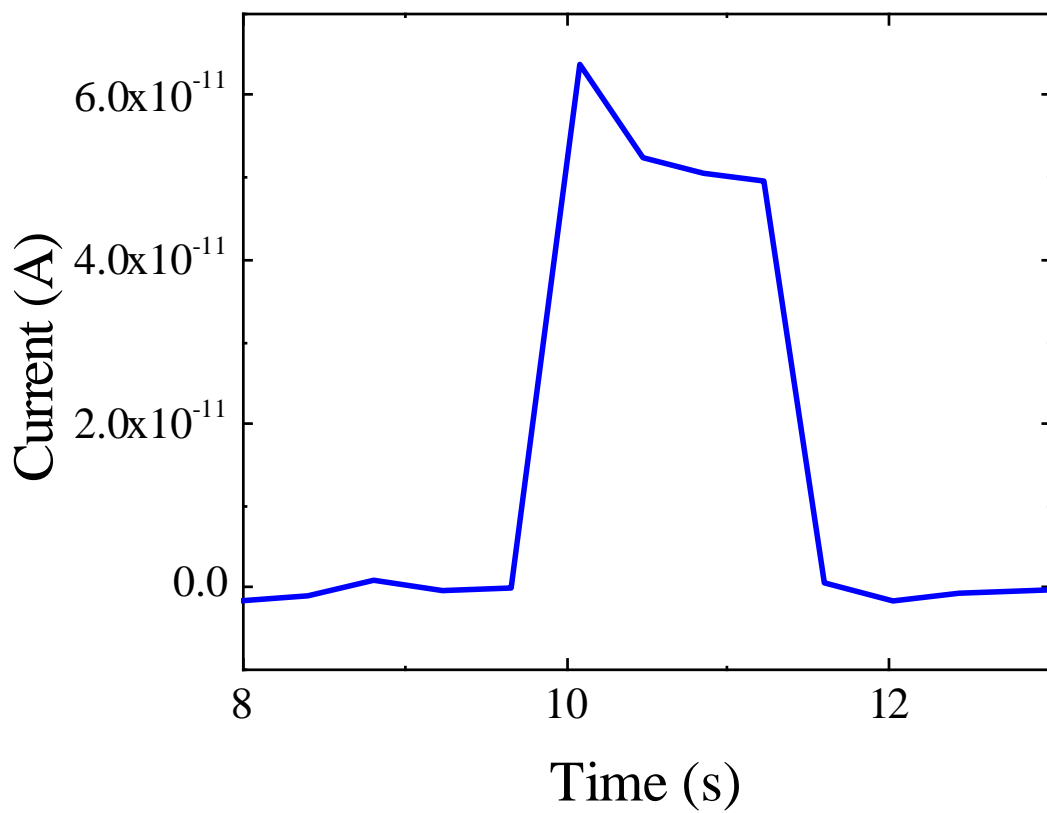Figure C.3. The Time-resolved current response of the Au/CuO/Ti device at 5 V.

Figure C.4. The Time-resolved current response of the Au/CuO/Ti device at 0 V.

Appendix D: Characterization Tools

UV-Vis spectroscopy

In this project, the Cary 500 UV-Vis spectrophotometer is used to characterize the absorbance spectra of synthesized materials in the form of liquid or solid thin films. This instrument covers the spectrum range of 175 to 3300 nm. The absorbance spectra provide useful information regarding the excitonic peaks and bandgap of materials. The Tauc plot is used to determine the bandgap of synthesized materials. The absorbance is given by Beer-Lambert law,

$$I = I_0 \ e^{-\alpha d}$$

Where I_0 is the incident light intensity, I is the transmitted light intensity through the material, d is the optical path length of the sample, and α is the absorbance coefficient. Therefore, the absorbance A is given by $A = \ln (I/I_0)$ with an arbitrary unit.
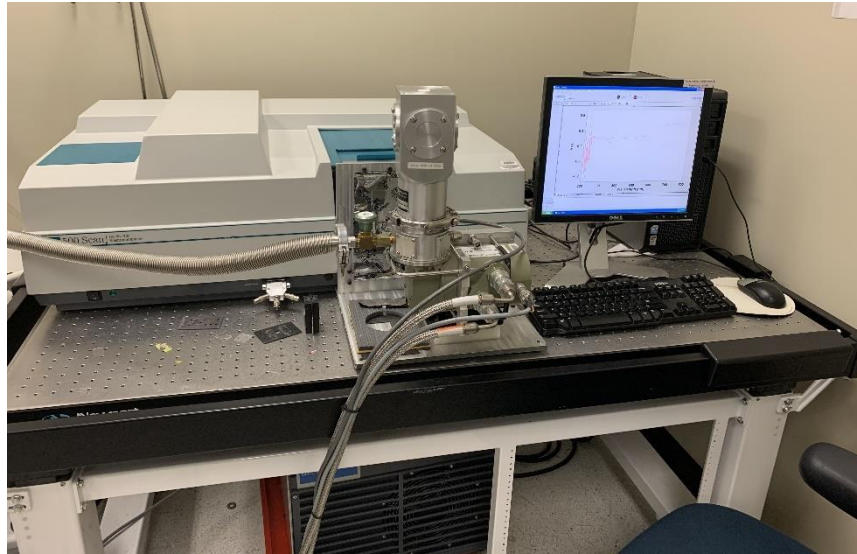

Figure D.1. A picture of Cary 500 UV-Vis spectrometer located in the optoelectronic lab, "Photo by Amir Shariffar"

Photoluminescence

Photoluminescence (PL) is an optical phenomenon in a semiconductor. First, the incident photons with energy higher than the bandgap of the material are absorbed, and electron-hole pairs are generated. Second, the excited electrons return to the ground state and emit photons corresponding to the bandgap of the material. PL measurements are performed to probe radiative recombination in semiconductors. The PL spectra provide useful information regarding the quality of the material, full width at half maximum (FWHM), and the bandgap of the material. The Horiba LabRAM spectrophotometer is equipped with a Synapse CCD detector which is cooled to $-70\,^{\circ}C$ during measurements. A 632 nm red or 472 nm blue continuous lasers are used to excite the materials in the form of thin films. The incident laser power is adjustable by selecting appropriate density filters. The laser light is focused onto the sample using an appropriate objective and slit size. The emitted light from the sample is reflected and guided through the Vis-IR bandpass filter and a 500 nm cut-off filter.

Figure D.2. A picture of Horiba LabRAM spectrometer located in the optoelectronic lab, "Photo by Amir Shariffar"

Raman spectroscopy

Raman spectroscopy is a characterization method to determine the optical phonon modes of a material. The Horiba LabRAM spectrophotometer is used to determine the optical phonon modes of the material. A 632 nm red or 472 nm blue continuous lasers are used to excite the materials in the form of thin films. The incident laser power is adjustable by selecting appropriate density filters. The laser light is focused onto the sample using an appropriate objective and slit size. The intensity of inelastically reflected light is significantly less than the elastically reflected light. Thus, the emitted light from the sample is reflected and guided through the notch filter to remove the elastically scattered light. Raman spectroscopy was used in this project to confirm the presence of specific materials components by comparing the position of phonon modes with the existing literature.

X-ray Diffraction (XRD)

X-ray diffraction or XRD is a characterization method to determine the elements, lattice spacing, and crystalline quality of the materials. A beam of high-energy X-ray hits the sample at a given range of angles, then the scattered light from different planes of the crystal undergoes either constructive or destructive interference, which determines a diffraction pattern. The diffraction peaks position and intensity are analyzed to determine the elements and crystal structure. This concept is explained using Bragg's law,

$$2d \sin \theta = n\lambda$$

Where d is the lattice spacing, θ is the scattering angle, n is a positive integer, and λ is the incident wavelength of the light. In this project, the Rigaku Miniflex X-ray diffractometer is used to determine the crystalline quality of materials and compare constituting elements of quantum dots and thin films.

Figure D.3. A picture of Rigaku Miniflex X-ray diffractometer located in the optoelectronic lab, "Photo by Amir Shariffar"

Scanning Electron Microscopy (SEM)

Scanning electron microscopy (SEM) is used to investigate nanostructures in detail. A beam of primary electrons scans the sample, the scattered secondary electrons are collected to form an image. In this project, we used the FEI Nova Nanolab 200 for advanced measurements of quantum dots and thin films. The Nova Nanolab is a Dual-Beam workstation with a FEG Scanning Electron Microscope and a Focused Ion Beam.

Figure D.4. A picture of the FEI Nova Nanolab 200 located in the optoelectronic lab, "Photo by Amir Shariffar"

Photolithography

The standard photolithography process is used to fabricate interdigital devices with different dimensions. The substrate is rinsed ultrasonically using isopropanol, acetone, methanol, and deionized water. Then, a few drops of the positive photoresist (AZ®P4330) are spin-coated onto the sample at 3000 rpm for 30 seconds. The photoresist thin film is annealed at 110 ℃ for 3 minutes. The prepared samples are aligned under the photomask and exposed to UV light to achieve the desired interdigital pattern. After the UV exposure, the samples are immediately taken into the developer (AZ®400K) for 45 to 50 seconds. Finally, the sample is dipped into the DI water. The obtained structure is investigated using a microscope to ensure that the developing process has been successful. Following this process, the samples are loaded into the chamber of the Angstrom Nexdep electron beam evaporator for metallization. Depending on the device, gold, chromium, copper, nickel, titanium, aluminum, and silver can be deposited onto the sample at the desired deposition rate and thickness. Finally, the lift-off process is performed to remove the photoresist and achieve the patterned device.

Figure D.5. A microscopic picture of the fabricated interdigital device (finger-spacing: 50 µm), "Photo by Amir Shariffar"

Current-Voltage (I-V) Characterization

The current-voltage (I-V) curve of all the devices were characterized using a Keithley 4200 parameter analyzer equipped with two SMU units and 4200-PA preamplifiers. In this research, the voltage sweep was used as the input source, and it was limited between -5 and 5 V. The output current was measured under the current compliance of 0.1 A. The current time-resolved measurements were performed at a specific bias voltage, and the current was recorded while the input light was manually turned on and off. The logarithmic scale was used to depict the significant differences in I-V results. The Keithley 4200 parameter analyzer can be connected to a probe station for precise memristive I-V characterizations.

Figure D.6. A picture of the Keithley 4200 parameter analyzer (left) and a solar simulator (right) located in the optoelectronic lab, "Photo by Amir Shariffar"